FINAL REPORT

Report Submitted to:	**Office of Naval Research**
Project Title:	**Efficient Acoustic-Optical Fiber Coupling for Enhanced Sensor Response**
Principal Investigator:	**Dr. Gary Pickrell** **Professor of Materials Science and Engineering** **pickrell@vt.edu** **(540) 231-3504**
Award Number:	**N00014-20-1-2485**
Report Submission Date:	**August 18th, 2023**
Recipient Organization:	**Virginia Polytechnic Institute & State University** **Office of Sponsored Programs** **300 Turner St NW, NEC Suite 4200** **Blacksburg, VA 24061**
Reporting Period:	**April 20, 2020 – April 19, 2023**
Project Grant Period:	**April 20, 2020 – April 19, 2023**
Report Period End Date:	**April 19, 2023**
Report Term:	**Final**

CPT
CENTER FOR PHOTONICS TECHNOLOGY

TABLE OF CONTENTS

1 DISTRIBUTION STATEMENT

DISTRIBUTION A. Approved for public release: distribution unlimited.

2 EXECUTIVE SUMMARY

In this three-year program, the research team designed, fabricated, characterized and optimized acoustic couplers for the distributed fiber optic acoustic sensing systems. Exhaustive theoretical analyses and experimental work was performed to evaluate a number of different designs to include metallic and fused silica splayed fiber coupler, tapered fiber couplers, split, side-slot, biconical and bi-exponential and wire horn couplers; multiple welding, polishing and adhesive techniques were also investigated. An improved FBG-based acoustic detection system was designed and constructed for automatic environmental compensation and advanced signal processing schemes were demonstrated to enhance acoustic detection. A 2.7 times coupling efficiency enhancement was demonstrated with a metallic splayed wire coupler. All milestones were met and two intellectual property disclosures were submitted to Virginia Tech Intellectual Properties (VTIP) for consideration for filing with the United States Patent Office.

3 ACCOMPLISHMENTS

3.1 Project Goals and Objectives

The *original* objective of the proposed three-year effort was to develop compact and efficient acoustic optical fiber horns and couplers and demonstrate improvements to the ultrasonic detection sensitivity of fiber Bragg grating (FBG) sensors. Exhaustive theoretical modeling and analyses were performed to design acoustic-optical horns and couplers for mode conversion and propagation in fused silica optical fibers. Materials optimization was performed on selected acoustic-optical fiber horn/couplers that will be fabricated and integrated with the sensing fiber. Materials and techniques were evaluated to bond the horn/amplifier to the surface of the test piece and embedded in a test piece. A preliminary investigation of lamb wave coupling efficiencies to a fused silica optical fiber and single crystal sapphire fiber based ultrasonic coupling to silica based optical fiber was performed. The performance and coupling efficiencies of the horns/couplers were characterized with our unique in-house characterization equipment that enables attenuation and power confinement via time domain reflectometry (TDR). An acoustic sensing system was developed to demonstrate the real-time interrogation of three ultrasonic sensors with high detection sensitivity. The goals and objectives were refined over the duration of the project and the research team consistently adapted to ensure project success.

3.2 Tasks Completed

To meet the project goals and objectives the following tasks were completed during this project.

- Proposed splayed fiber acoustic coupler and demonstrated the potential for energy-conservation-limited amplification within broad frequency range.
- Fabricated all-silica splayed fiber couplers and verified the theoretically predicted square-root law relations.

- Fabricated metallic splayed wire coupler and demonstrated a 2.7 times coupling efficiency enhancement.
- Investigated and developed multiple welding and adhesive techniques for coupling along a non-terminated optical fiber.
- Investigated and attempted fabrication of EDM wire for tapered trench fabrication.
- Fabricated a tapered fiber coupler using a simple polishing method.
- Designed an improved FBG-based acoustic detection system including a LabVIEW-based control system for automatic environmental compensation.
- Simulated split horn coupler and direct wire-to-fiber coupling using COMSOL to understand the coupling mechanism, select ideal parameters, and realize the importance of adding a back-horn to the design.
- Simulated dual horn structure and investigated the coupling efficiency dependency on different tapering profiles including biconical horn and bi-exponential horn designs.
- Fabricated multiple iterations of the new split horn and side slot horn approach to acoustic coupling, which has the ability for future simple and robust field installation, as well as axial strain enhancement within the optical fiber.
- Investigated new signal manipulation and processing-based methods for acoustic enhancement with the goal of reducing sensitivity to variation fabricated tolerances.
- Proposed wire horn structure which allows high fabrication and implementation tolerances.
- Simulated and fabricated multiple designs of the wire horns, which shows efficient enhancement of the acoustic energy transmission from the acoustic waveguide to optical fiber. The one-piece wire horn structure shows good ability for simple in-the-field implementation.

3.3 Results and Discussion

3.3.1 Theoretical Modeling of the Splayed Fiber Coupler

A splayed fiber coupler was investigated for its potential coupling improvements over a single fiber remotely bonded from a sensing fiber Bragg grating (FBG), as illustrated conceptually in Figure 1. The coupler consists of a single fiber splayed into several identical fibers, with the splayed fibers bonded on a surface where the acoustic emission needs to be detected. Once acoustic waves enter the bonded part, their energy will be coupled into the splayed fibers, and then merged

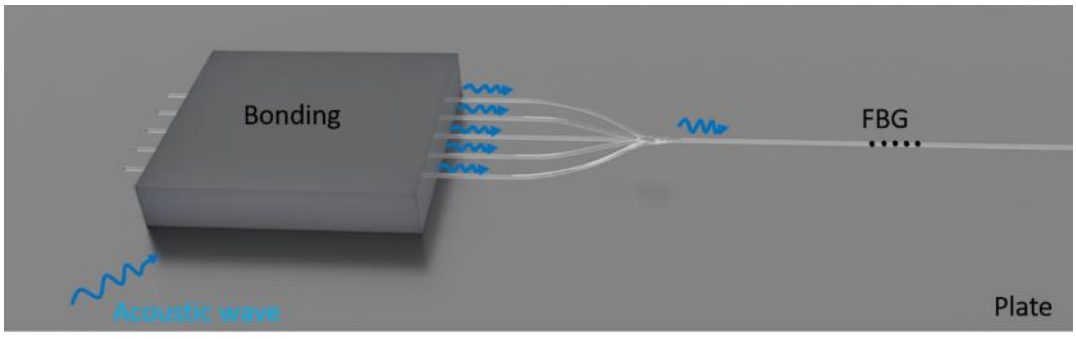

Figure 1. Illustration of the splayed fiber coupler design.

into the single fiber section that is measured later by a fiber sensing element. Because of the increased number of acoustic energy acceptors, the received acoustic signal is expected to be enhanced compared to the scenario where only a single fiber is used. In addition, due to the low propagation loss of acoustic waves in fused silica, the emitted acoustic wave can be routed out and measured at a distant location, enabling flexible configurations.

An example of the geometry and dimensions used in the analysis is shown in Figure 2. For simplicity, the joint was set flat, and the transition region was generated automatically by the loft function in a CAD software (Autodesk Fusion 360). All fibers are fused silica with a 125 μm diameter and the splayed fibers have equal lengths. Since the difference of acoustic properties

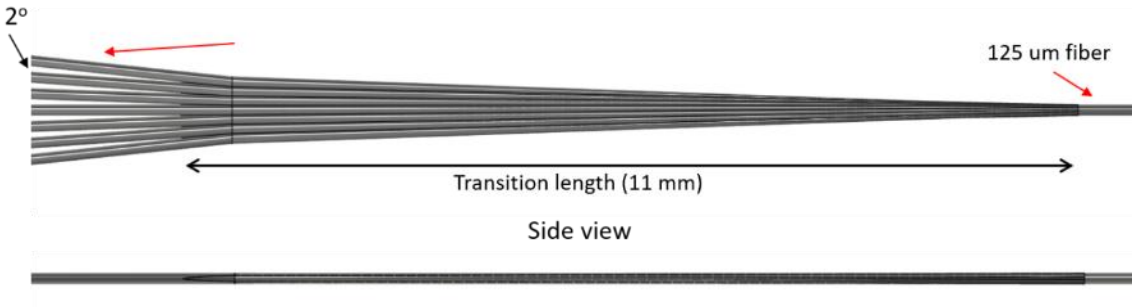

Figure 2. Geometry and dimensions used in the simulation (7 fibers shown as an example).

between the Ge-doped optical core and pure silica cladding is negligible, the fibers were set as homogenous in the analysis. To minimize any unwanted reflections from abrupt changes of structural dimensions, the transition region was designed to be adiabatic. Therefore, the angle between splayed fibers was set at 2 degrees, and the transition length was 11 mm. The structure was analyzed via numerical simulation with COMSOL Multiphysics. Considering that FBGs are going to be used as the sensing elements, the axial strain induced by the acoustic wave was evaluated. Since, in most cases, FBGs are only sensitive to longitudinal acoustic waves along the fiber axis, all excitation used in the simulation was longitudinal.

To better characterize the structure, the splayed fiber was parameterized based on its geometry and the physical process, as shown in Figure 3. The splayed fiber coupler can be viewed as a multi-port device. An *N*-port splayed fiber coupler has a total of *N*+1 ports. Since in the application there

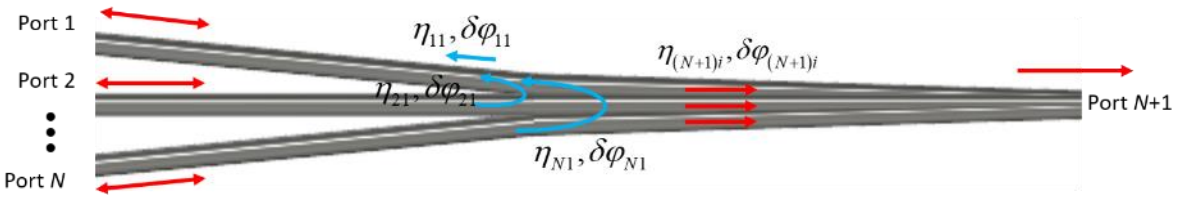

Figure 3. Port labeling and parameter definitions.

is no acoustic wave from port *N*+1, port 1 to *N* are defined as bi-directional ports and port *N*+1 has only a single direction. When an acoustic wave is input into port i (i = 1, 2, …, N), it propagates along the arm and reaches the joint. Since there is a discontinuity at the joint, some energy will be reflected. Besides reflection, some energy will also be coupled to other ports. For generality, the coupling efficiency and phase shift are defined as $\eta_{ij}$and $\delta\varphi_{ij}$, respectively. Equal subscripts refer to the case of self-reflection and i = N+1 represents transmission. To characterize $\eta_{ij}$and $\delta\varphi_{ij}$,

simulations were run by single excitation port by port, and with different values of N. By examining the results, an empirical expression was obtained for when the acoustic wavelength is much longer than the physical dimension of the joint (equal-phase assumption).

$$\eta_{ij} = \begin{cases} \sum_{j \neq i}^{N} \eta_{ij} \;\; i, j = 1, 2 \ldots N, \\ \dfrac{1}{\sqrt{N}} \; i = N+1, \end{cases} \qquad \delta\varphi_{ij} = \begin{cases} \pi \;\; i = j \\ 0 \;\; i \neq j \end{cases} \tag{0.1}$$

The expression can be interpreted as follows. The self-reflected wave will interfere with the cross-coupled wave destructively, and, if all of the inputs are equal, the interference will be perfect, and no wave will exit from port 1 to N. On the other hand, all waves transmitted to port N+1 interfere constructively. However, with an increasing number of ports, the single-port transmittance decreases and follows a square-root law. Therefore, the overall transmittance of the splayed fiber coupler, T_N, satisfies the following inequality, with equality only achievable when all inputs are identical. The proof of Eq. (0.2) can be easily derived from the Cauchy-Schwarz inequality.

$$T_N = \sqrt{\frac{\left| \sum_{i=1}^{N} \frac{1}{\sqrt{N}} u_i \right|^2}{\sum_{i=1}^{N} |u_i|^2}} \leq 1 \tag{0.2}$$

Here, u_i represents the input acoustic displacement field amplitude form port i. If all inputs are equal in both amplitude and phase, the amplification can be defined and calculated by normalizing the measured strain amplitude to that of the single-fiber scenario. The result is plotted in Figure 4. For 1 MHz excitation, the trend follows a square-root relation very well. For 500 kHz excitation, there is slightly lower amplification, which will be explained in a later section. The square-root law originates from the energy conservation and energy-strain relation in elastic materials. The

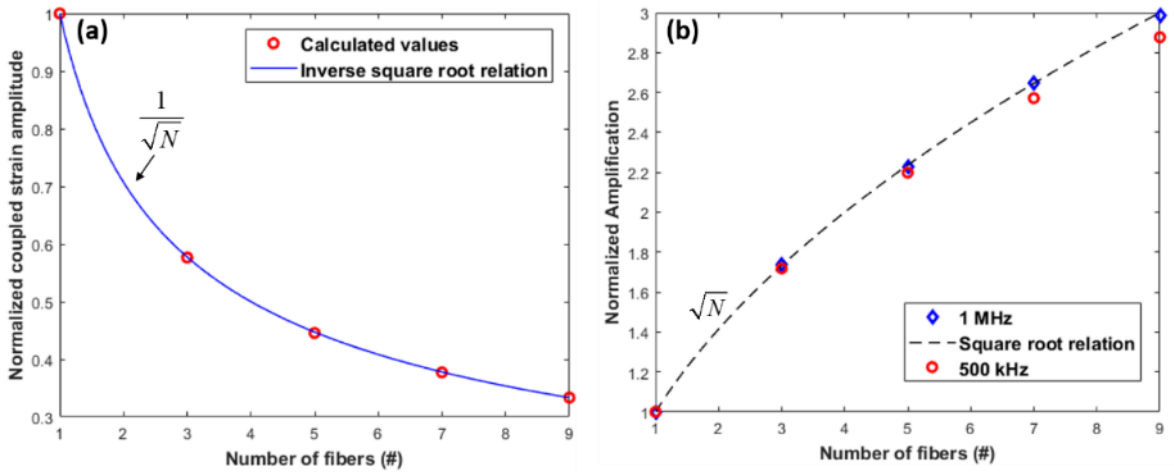

Figure 4. (a) Simulated normalized single-port transmittance with respect to port numbers. (b) Simulated normalized amplification with respect to port numbers.

acoustic energy is proportional to the square of the amplitude of the displacement field, which is proportional to strain.

The frequency response of the splayed fiber coupler was also investigated, and the simulation results are plotted in Figure 5. There is a broadband region where the amplification follows

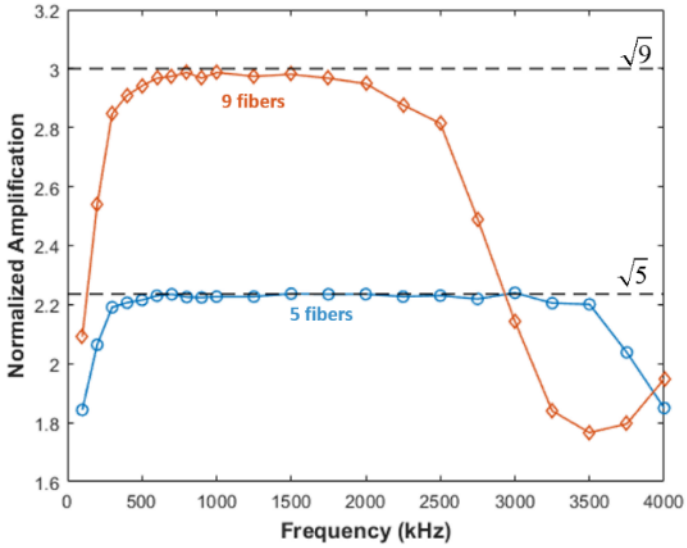

Figure 5. Frequency dependent acoustic amplification for 5 and 9 fiber splayed fiber coupler.

previous analysis and exhibits energy-conservation-limited transmittance, but the behavior deviates in the low and high frequency ranges. In the low frequency range, more energy is coupled into flexural modes, which cannot be detected by the FBG. Therefore, part of the acoustic wave is lost in the measurement and results in reduced amplification. At the high frequency range, the equal phase assumption in Eq. (1.1) no longer holds due to the decreased acoustic wavelength. Therefore, the transmitted acoustic waves no longer interfere constructively, and the amplification is reduced. A greater number of fibers necessitates a larger physical dimension, and thus the cut-off frequency is lower. Moreover, the increased frequency also causes the transition region to start to operate in the multimode regime, and the additional phase discrepancies among the modes complicate the wave interference.

To ensure that the splayed fiber coupler excitation at the sensor is independent of the exciting port, the port dependence was characterized in simulation. This was accomplished by probing both axial and transverse strain for each port excited independently. The results are shown in Figure 6. All ports have very similar waveforms, including shape, amplitude, and phase under identical inputs for longitudinal mode excitation.

In actual fabrication, the joint geometry might not be well controlled. Thus, the performance of the splayed fiber coupler with different joint geometries were investigated. Two other types of joints, illustrated in Figure 7, were analyzed. Their performance is very similar to the flat joint within the frequency range that satisfies the equal-phase approximation. The reason is that, under this approximation, the joint is treated equivalently to a single point, and therefore its geometry does not make any difference.

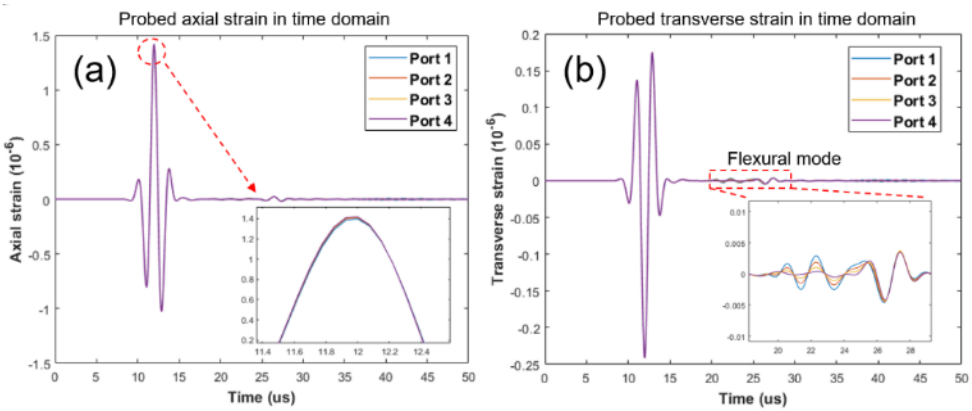

Figure 6. (a) Simulated sensor axial strain dependence on port excitation. (b) Simulated sensor transverse strain dependence on port excitation.

Figure 7. Two other types of joints investigated in the analysis.

In conclusion, the numerical evaluation of the splayed fiber coupler indicates its capability to achieve energy-conservation-limited amplification within a broad frequency range. This structure can also be used as an acoustic router to guide acoustic waves from different arms into a single fiber, but the transmittance for a single port is decreased with increased fiber numbers.

3.3.2 Fabrication and Characterization of Splayed Couplers

To evaluate the accuracy of the theoretical analyses, an all-silica and metallic coupler was fabricated and characterized.

3.3.2.1 All-Silica Coupler Fabrication and Characterization

Beyond theoretical analysis and modeling, we also developed a method for fabricating splayed fiber couplers, as shown in Figure 8. The fibers are twisted together and mounted on two fiber holders. A propane/oxygen torch is used to heat the fiber beyond its softening point. Concurrently, the fibers are stretched so that they are fused together and tapered down to a single fiber diameter. Afterwards, the fused fiber taper is cleaved at the center point and spliced to a single fiber with a conventional arc fusion splicer. A representative photograph of the fabricated splayed fiber (N =2) is shown in Figure 8(c). These methods were employed to fabricate up to 7 splayed fibers, which can be seen in Figure 9. The number of fibers is limited by the fiber clamping method rather than the procedure. The results confirm the anticipated amplification for up to 5 fibers. Importantly, the signal features for all couplers are similar, as shown in Figure 10.

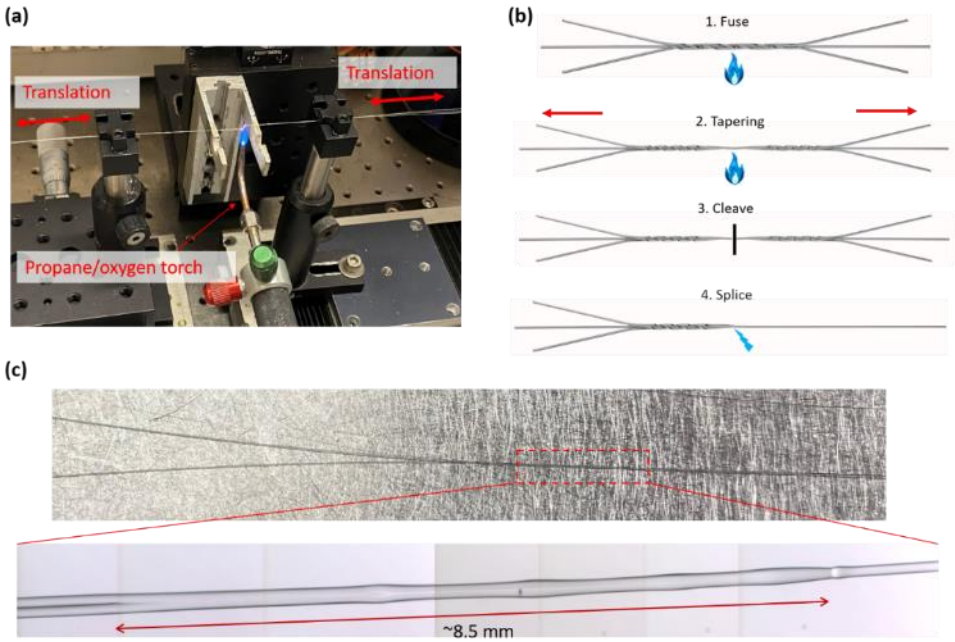

Figure 8. Setup (a) and fabrication procedure (b) for splayed fiber coupler. (c) Picture of a fabricated splayed fiber coupler (N=2).

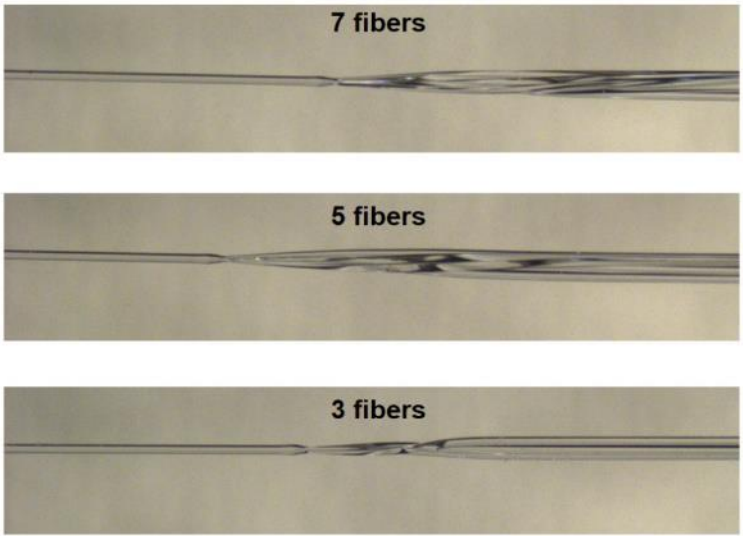

Figure 9. Different numbers of silica splayed fibers fabricated with repeatable results.

It was also found that different numbers of fiber have different responses with respect to applied force in the mechanical coupling. This is likely due to different deformation geometries of the force-applying foam. For better evaluation, the averaged amplitudes within a force range were measured. As shown in Figure 11, the measured enhancement yields a trend similar to the theoretical predicted square-root law relation

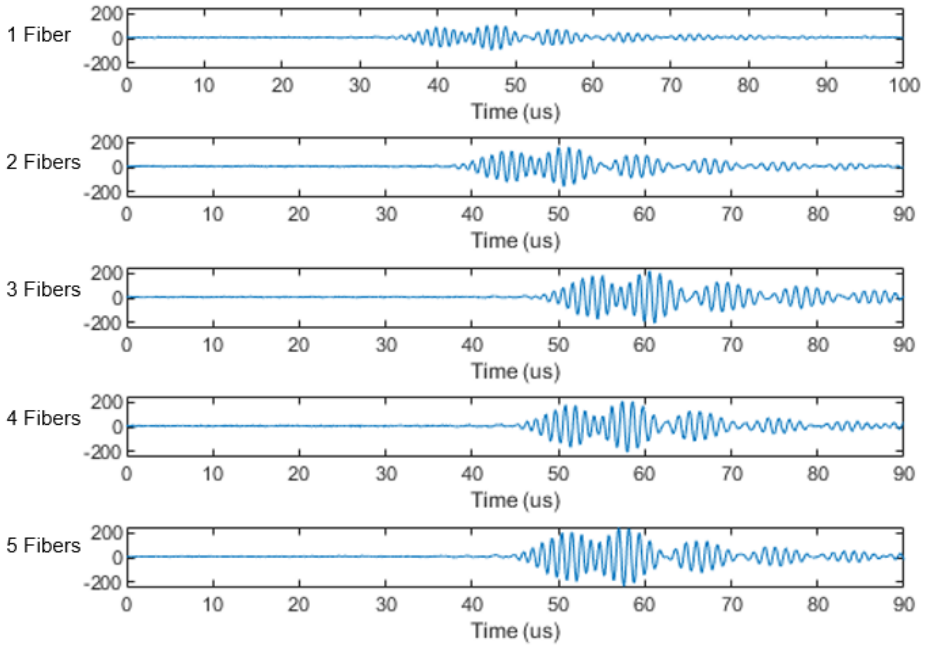

Figure 10. Silica splayed fiber initial results, showing similar waveforms for different numbers of fibers. Different numbers of silica splayed fibers fabricated with repeatable results.

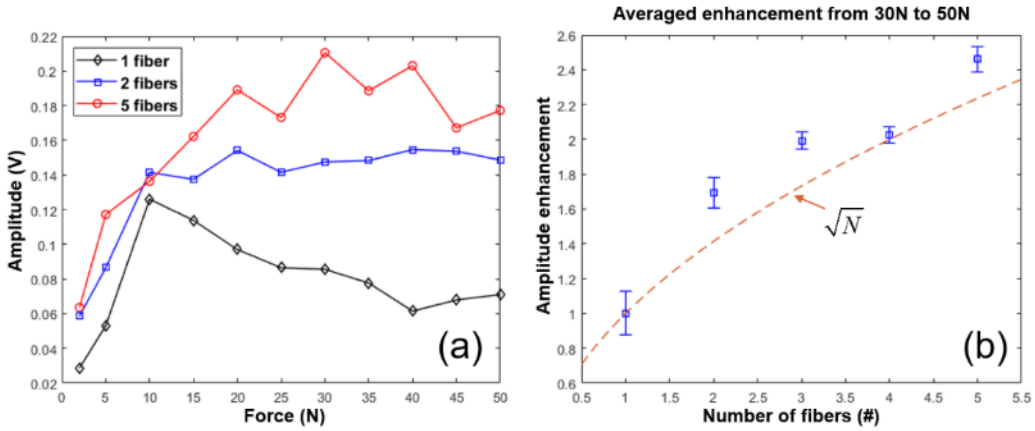

Figure 11. (a) Relationship of applied mechanical clamping force with acoustic coupling efficiency for different splayed fiber numbers. (b) Relationship between splayed fiber number and acoustic coupling enhancement when averaged over a range of mechanical coupling forces.

3.3.3 Metallic Splayed Wire Coupler Fabrication and Characterization

An additional method for splayed fiber coupling to an optical sensor was investigated in fabrication and initial tests. Instead of splaying a single optical fiber into multiple silica fibers, we instead splay an aluminum wire into multiple aluminum wires and couple the aluminum wire to an optical fiber at the joint for optical-based detection. In the all-silica method, the acoustic impedance is matched at the splayed joint, but mismatched at the bonding point on the test piece. In this new method, there is an impedance match at the bonding point on the test piece (assuming aluminum

for investigative purposes), and an impedance mismatch at the splayed joint. Therefore, we can expect similar coupling efficiencies, but an easier fabrication procedure and an overall less fragile sensor.

In this method, we start by fusing the desired number of aluminum wires using a laser welder. This is shown in Fig. 12. The aluminum wires are held in place with a small glass tube, and irradiated with a 1070 nm laser. The molten aluminum flows, but is held in place by the tube, which acts as

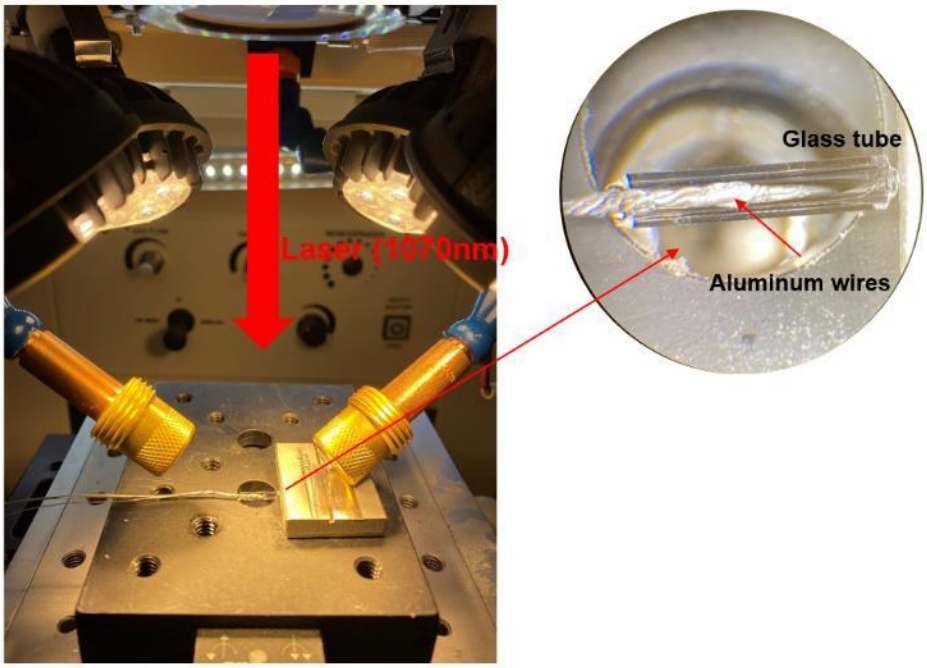

Figure 12. 1070 nm laser welding of several aluminum wires.

a cast. The glass tube is then cleanly removed by shattering gently with a hammer. A 1064 nm pulsed laser was then used to remove material from the aluminum joint. First, the joint is tapered to a fine point. The purpose of this is to have a transition region to match the silica optical fiber diameter. Then, a trench is cut into the joint, to securely hold the silica fiber once adhesive is cured and during curing. The silica fiber is held in place with a small amount of cyanoacrylate glue, as shown in Figure 13.

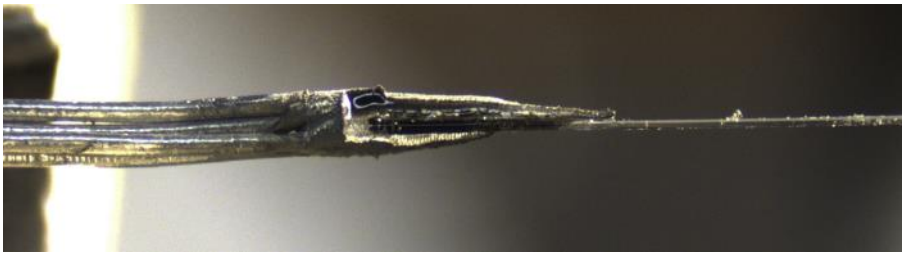

Figure 13. Silica fiber spliced to splayed aluminum acoustic coupler.

Initial results of the coupler show very good coupling efficiency and appear to be as good or better than the all-silica splayed coupler. We can see approximately 2.7 times coupling efficiency enhancement in Fig. 14(a), and very similar waveforms when each port is excited separately in

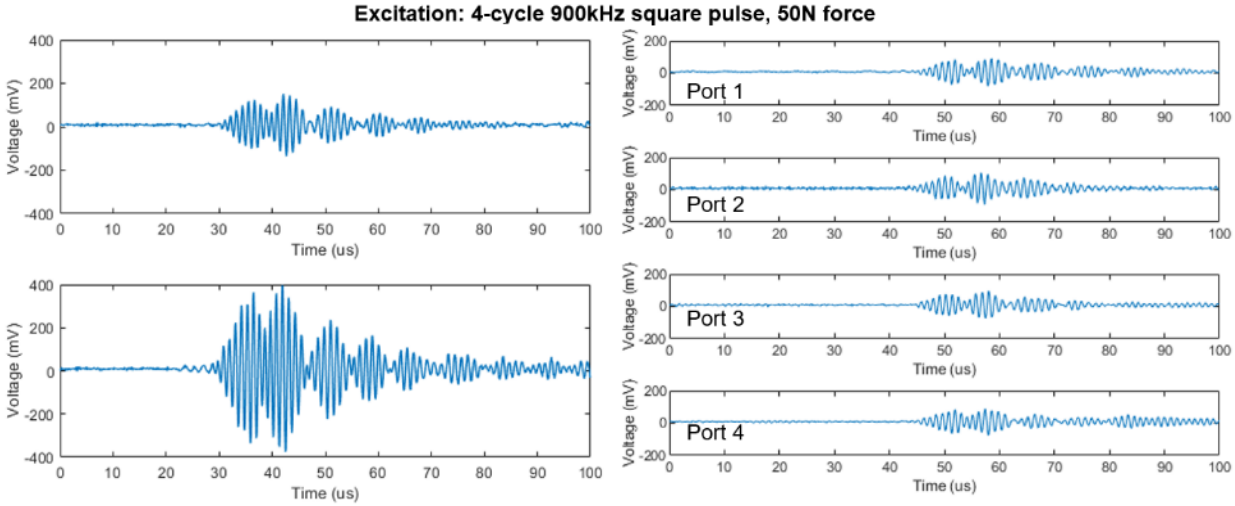

Figure 14. (a) Coupling efficiency enhancement (~2.7 times) from a *N* = 4 splayed aluminum acoustic coupler. (b) Similar waveform shapes from individual port excitations.

Fig. 14(b). The splayed metallic wire coupler, as shown in Figure 15, is extremely versatile and adaptable, and well suited for flat surfaces.

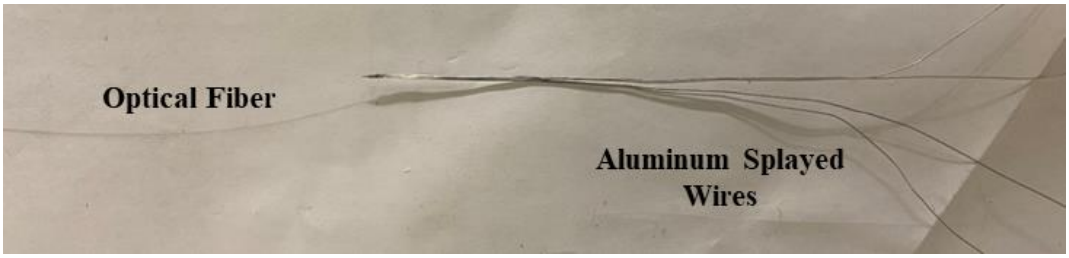

Figure 15. Aluminum splayed wires joined to silica fiber.

With the addition of a fluoride salt based flux, the fibers can now be fabricated without visible oxidation that causes structural weakening. The difference in quality can be seen in the microscope images in Figure 16. The floride salt based flux has a lower melting point than more traditional boric acid based fluxes, which works well with the relatively low melting point of alumium. Additionally, reduction of the oxide layer allows easier welding and the ability to directly weld the wires without the need for a glass tube cast to hold the molten aluminum.

3.3.4 Coupling of Sapphire Fiber to Metallic Splayed Wire Coupler

The splayed metal wire coupler is connected to a sapphire fiber with the previously described trench and adhesive method. The ability to transmit acoustic waves through this structure is compared to the transmitted power directly at the end of the splayed wire coupler. Additionally, the sapphire fiber is spliced to uncoated silica fiber using a low melting point glass as an adhesive during fusion splicing. This third structure is compared to the first two in terms of

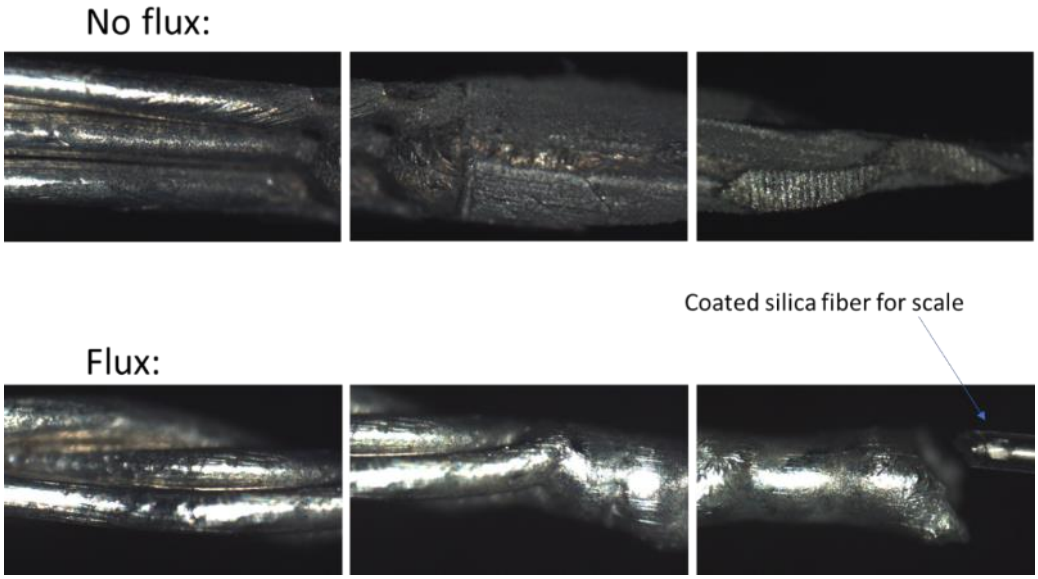

Figure 16. Effect of adding flux while soldering aluminum wires.

transmission. Figure 17 shows the test set-up where the splayed wire coupler is connected directly to a receiving transducer

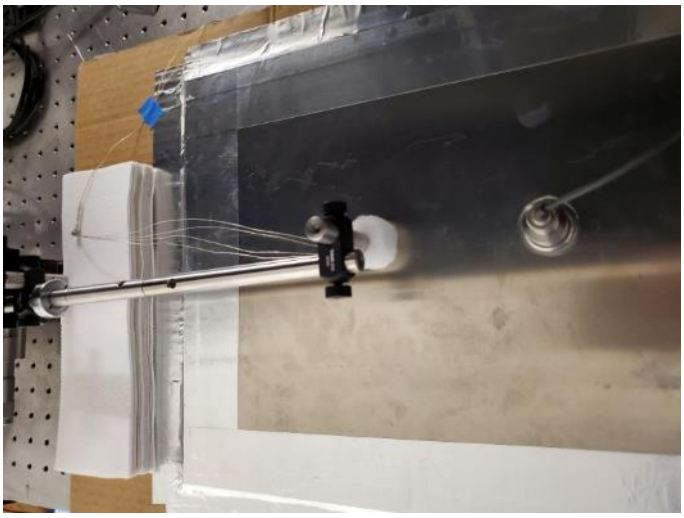

Figure 17. Splayed wire coupler receiving acoustic waves from the test piece and carrying them to a transducer.

The data is averaged 100 times in the *direct splayed-Al to transducer* trials, and 1000 times in both the *splayed-Al-sapphire-fiber to transducer* and *splayed-Al-sapphire-fiber-silica-fiber to transducer* trials. 10 trials are conducted for each configuration, where the coupler wires or fibers are unperturbed after each. In Figure 18, we can see the averaged results for the *direct splayed-Al to transducer* and the *splayed-Al-sapphire-fiber to transducer* configurations.

We normalize the transmitted peak power to the average peak power of the *direct splayed-Al to transducer* configuration. Then, the average transmitted peak power is 0 dB ($1\text{-}\sigma = 0.0153$ dB) for the *direct splayed-Al to transducer* configuration, -10.5 dB ($1\text{-}\sigma = 0.457$) for the *splayed-Al-*

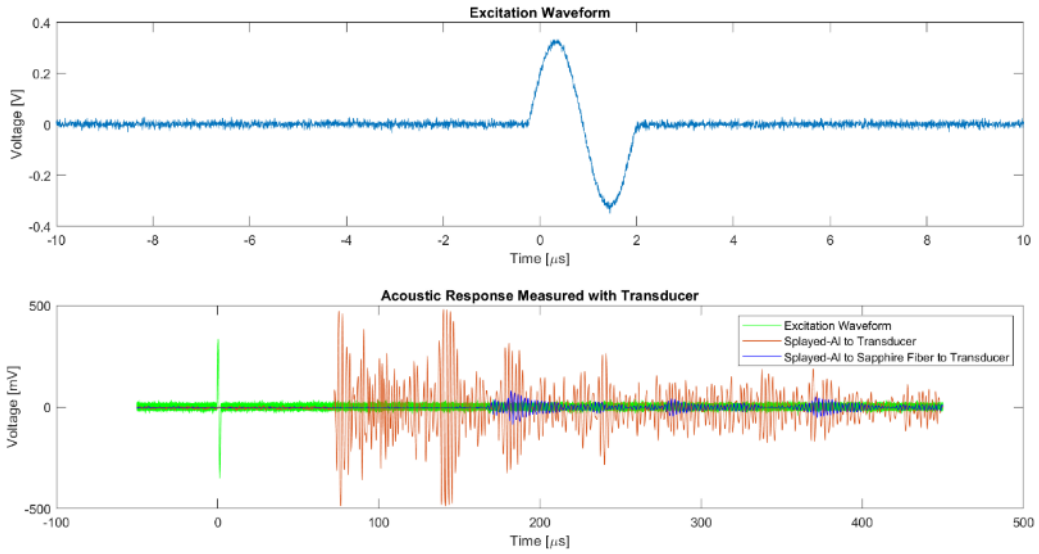

Figure 18. Excitation waveform from a transmitting transducer on test piece and the acoustic response measured with a receiving transducer.

sapphire-fiber to transducer configuration, and -11.8 dB (1-σ = 0.477 dB) for the *splayed-Al-sapphire-fiber-silica-fiber to transducer* configuration. Please note that several dB of the transmission loss are a result of the inability to keep the entire section of sapphire fiber suspended due to limitations of the test environment.

3.3.5 Investigation of Integrated Solid Horn Design

In addition to the previous design, we proposed a solid-horn fiber design, as shown in Figure 19, to enhance acoustic wave coupling. This structure consists of a fiber with diameter variation. The

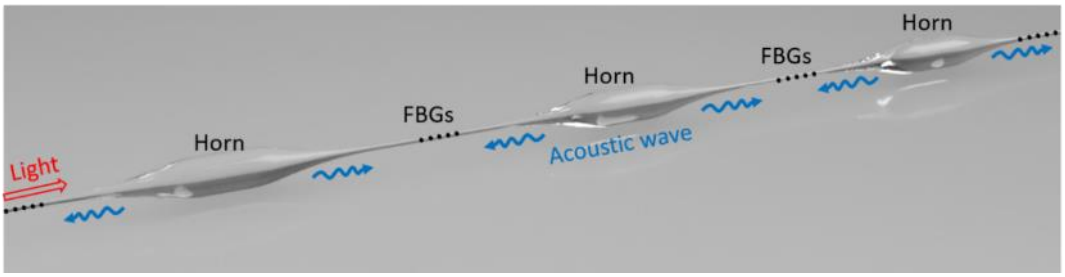

Figure 19. Illustration of the solid-horn integrated fiber design.

thicker parts serve as acoustic horns that collect the ambient acoustic wave and, therefore, the acoustic wave received in the thin fiber section is amplified. Numerical simulation was performed under two different scenarios: surface mount and embedding. In both cases, illustrated in Figure 20, the structure shows strong acoustic amplification compared to a single fiber in preliminary simulations. For example, for a 1 mm diameter horn, the amplification is about 5 times and 14 times for the surface mount and embedded configurations, respectively. The structure can also detect the acoustic wave that vibrates perpendicular to the fiber direction, which cannot be measured by a single fiber. A potential fabrication method was also proposed, as shown in Figure 21; during the fiber drawing process by varying the drawing speed.

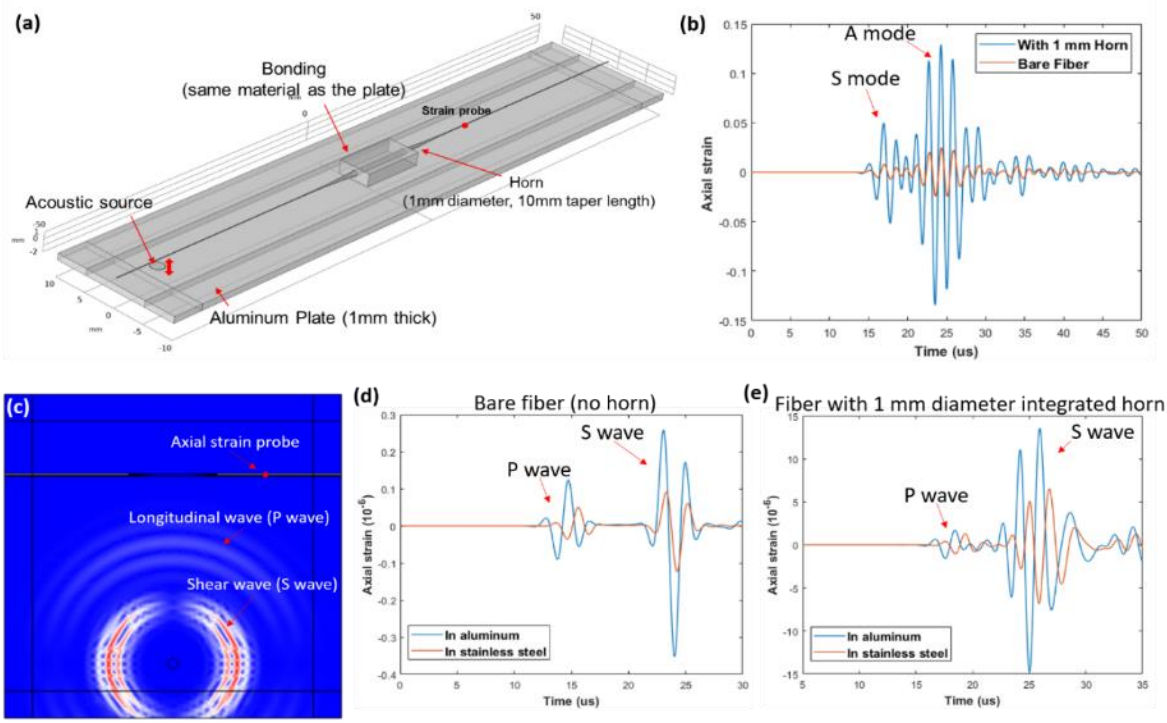

Figure 20. Simulation configuration and results for horn-integrated fiber under surface mount configuration (a)-(b) and embedded configuration (c)-(e).

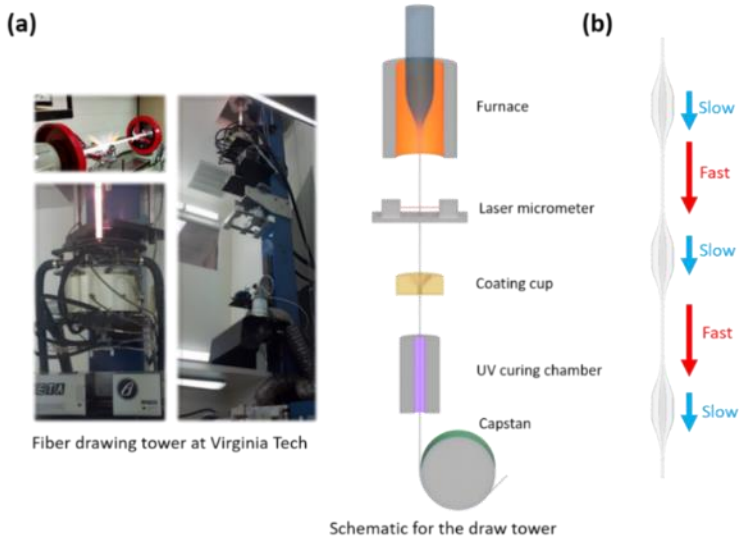

Figure 21. (a) Photograph and schematic drawing for the fiber drawing tower at Virginia Tech. (b) Method to fabricate horn integrated fiber.

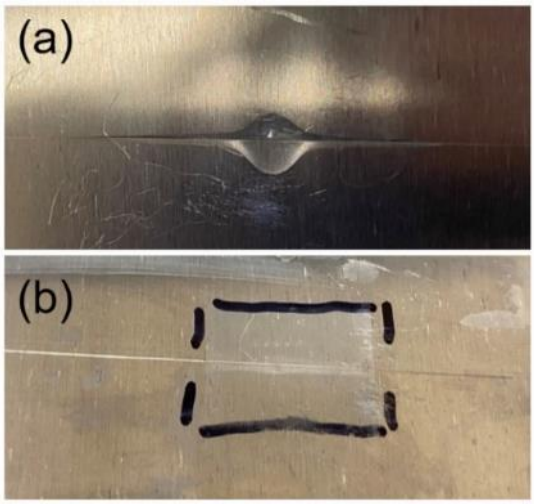

Figure 22. (a) Cyanoacrylate glue (pre-cure) flowing on fiber and test piece. (b) Cellophane tape securing fiber onto test piece.

3.3.6 Investigation of Mechanical Coupling Methods

The splayed fibers or other designs must be coupled to the test piece in some manner that can give repeatable results, and quantitatively compared. In an eventual application, the fibers or horns may be embedded directly into a metallic block, forming a composite material. This block can then be welded directly to the test piece. This sort of method, however, is not feasible for quick and consistent evaluation of many designs.

Cyanoacrylate glue is a common semi-permanent acoustic coupling method due to its rigidity and low acoustic loss. Due to its high fluidity, the glue tends to spread on the test piece and along the fiber. This means that the morphology of the cured glue is difficult to control, and repeatable results are difficult to obtain. Accelerators can be used for nearly instant curing, but the glue spreads so quickly that the cured shape remains uncertain. Cyanoacrylate (pre-cure) is shown in Figure 22(a) as an example.

Another commonly applied acoustic coupling method is the use of pressure-sensitive cellophane tape, an example of which is shown in Figure 22(b). This allows better control of the fiber couplant morphology, although it is predicable that the coupling efficiency may be worse due to a larger acoustic impedance mismatch, higher propagation loss, and less fiber surface area in contact.

A new mechanical coupling method was designed, as shown in Figure 23. Using this method, the contact area is well defined, the bonding force is well controlled, and the soft foam promotes uniform pressure distribution across an area much larger than the fiber.

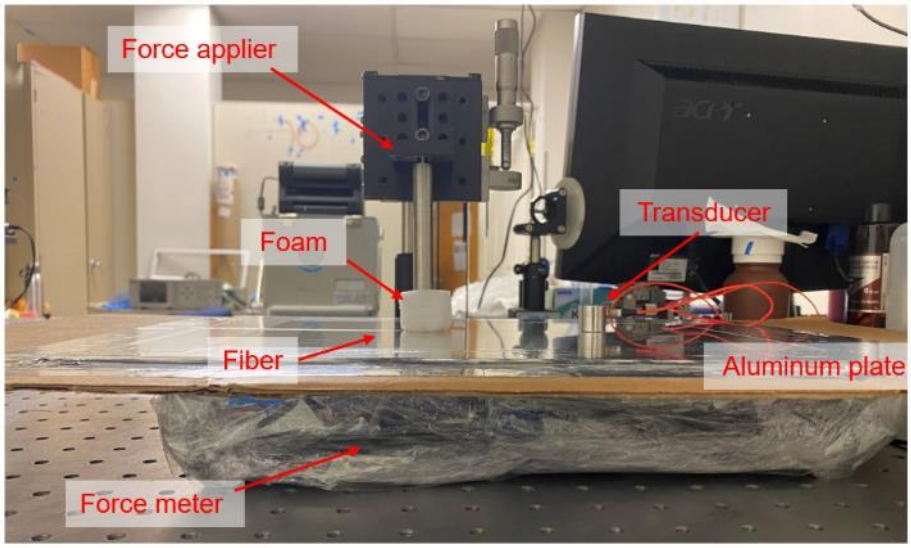

Figure 23. Uniform mechanical coupling method.

3.3.7 Improvements to Acoustic Detection

Detection of axial strain with an FBG is accomplished using a scheme similar to Figure 24. A combination of a super-luminescent diode (SLED) and a variable optical attenuator (VOA) allow the FBG spectrum to be monitored during the experiment. The SLED is switched off to reduce noise when the strain is being recorded. The tunable laser and VOA are adjusted to achieve high sensitivity with the FBG and high photodetector gain, respectively.

On the acoustic source side of Figure 24, a pulsed laser is used to excite high frequency acoustic waves, and a small amount of the pulsed laser energy is tapped to use as a trigger for the oscilloscope in detection.

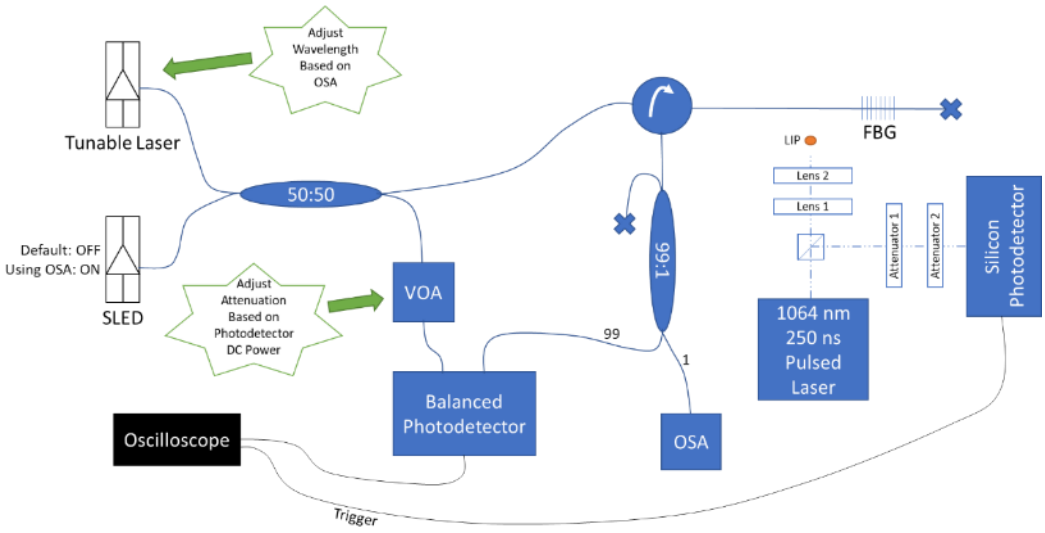

Figure 24. Acoustic detection using a tunable laser.

To determine the wavelength bias location of the tunable laser on the FBG, we calculate the maximum of the derivative of the FBG reflection spectrum. Point-by-point FBGs are sensitive to polarization, and therefore a compromise in ideal bias between polarizations is necessary. Additionally, nonlinearity in FBG reflectivity and environmental bias drift create an additional concern for biasing to steep portions of the reflection spectrum.

3.3.8 Investigation of Different Coupling Methodologies

The splayed coupler structure discussed in previous sections shows efficient acoustic coupling and has potential to achieve acoustic coupling to the energy conservation limit. However, the coupling structure requires truncation of the fiber. To allow distributive and remote sensing for the field applications, several new coupling structures which allow continuous fibers are proposed here.

Coupling the most acoustic power into an optical fiber as efficiently as possible lends itself to two principal approaches: (1) minimize the discontinuity and impedance mismatch between the acoustic waveguide and the optical fiber by creating a very small joint or (2) guide the acoustic wave into a larger structure that can then accomplish the same impedance matching but at a more manageable scale. The former approach leads to the premise of slotting or polishing the aluminum wire so that it can fit snugly together with the optical fiber and latter approach leads to the methodologies employed for acoustic horn. A comprehensive evaluation of both schemes has been accomplished during this project.

3.3.8.1 EDM-based Slotting

To achieve improved acoustic coupling to an optical fiber, attempts were made to machine an optical fiber-sized slot into the aluminum wire to house the fiber. One way to accomplish this is to use electrical discharge machining (EDM) with a cutting wire sized equal to the polyimide-coated fiber, i.e. 150 μm. The aluminum wire can be embedded in a metal block by first slotting parallel to the surface. After embedding with an adhesive, the metal block is rotated several degrees and the aluminum wire is slotted. The metal block can then be kept as a convenient holder for attaching

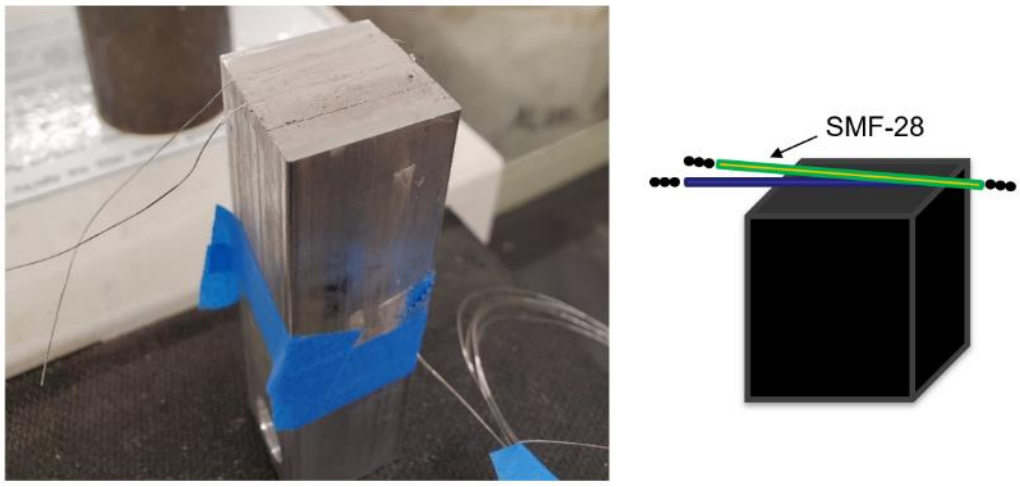

Figure 25. Process of EDM slotting a metal wire.

the optical fiber at the correct angle in the slot. Figure 25 shows the fixture containing optical fiber-sized wires as well as a depiction of the process of embedding the optical fiber into the fixture.

Unfortunately, implementation of this approach is hindered by several challenges. First, unlike many other pieces of machinery, we have no direct access to EDM equipment, and since this design requires many iterations, this leads to a significantly slowed timeline. Next, the adhesive that holds the metal wire in the slot must be conducting, or the slot will be low quality and automated machinery will simply refuse to finish the cut. Finally, EDM does not handle complex interfaces well, which will lead to the wire being quickly destroyed as it cannot dissipate heat while the cutting wire is still cutting into the block.

3.3.8.2 Tapered Waveguide Fabrication

Under the same premise as the EDM-based slotting, we attempted to polish the fiber down to an angle so that the coupling region reflection could be minimized. As we had shown previously, an asymmetric coupling region will result in a significant reflection from the interface and lower coupling efficiency in the forward direction. Although a large joint will also result in a larger reflection, we can solve one of these problems, even with asymmetry, by simply polishing the fiber into a thin wedge. This forces a large interaction region between the optical fiber and the aluminum waveguide, but a large reflection and non-ideal coupling was anticipated because the shear components in the coupling region cannot be canceled by symmetry. The polishing method, as shown in Figure 26, includes the fiber fixture and the polishing plate. The fiber fixture consists of a round cylinder which can hold the fiber with the aid of some phenyl salicylate and be polished flush against the polishing plate. The result is removing fiber material tangent to the cylinder, creating a taper with a taper rate dictated by the cylinder's diameter.

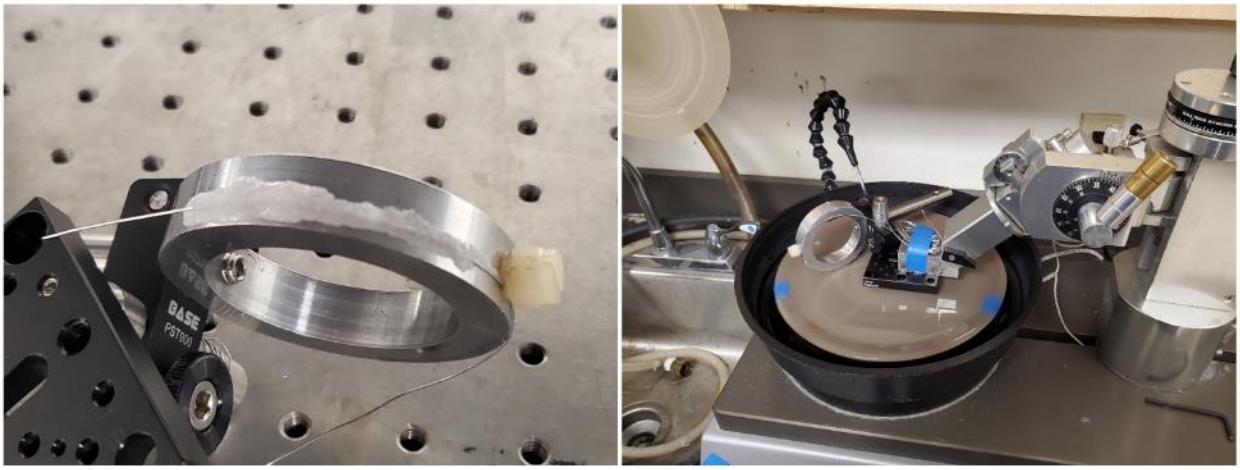

Figure 16. Polishing apparatus for tapering the aluminum wire.

The tapered aluminum wire was directly bonded to the optical fiber using phenyl salicylate. No difference in coupling efficiency was observed as compared to a flatly cleaved aluminum wire. Conversely a difference in waveform was observed in the time-domain, which we attribute to differences in adhesive geometry between trials. The relatively large amount of adhesive likely prohibits a meaningful difference in coupling quality in this comparison, but structural integrity of the coupling region seems to require this amount of adhesive.

3.3.8.3 Design of a Horn

A horn is designed to efficiently accomplish impedance matching between the aluminum wire acoustic waveguide and the optical fiber. The initial design was to have the fiber run through the center of the horn, which is comprised of two halves, and therefore called a split horn. The back of the horn is flat but allows multiple acoustic waveguides to be inserted symmetrically into holes. This allows both multiplexing or highly efficient coupling from a single source if phase matching can be accomplished by matching the wire lengths. This design is depicted in Figure 27.

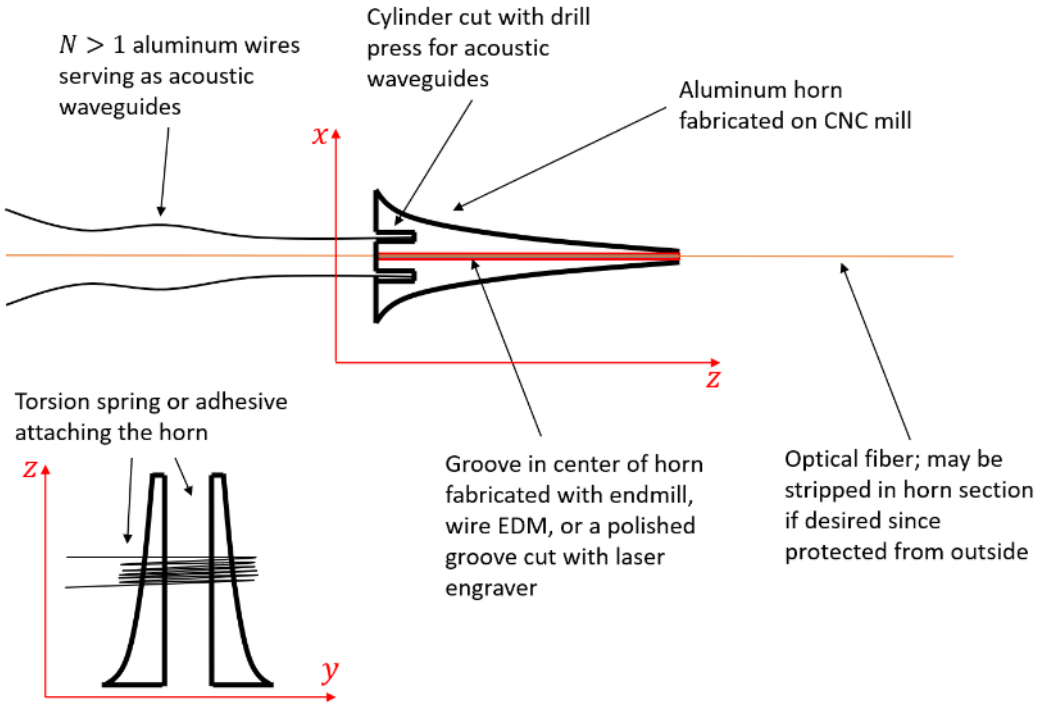

Figure 27. Diagram of the original split horn.

Initial attempts to fabricate this horn were challenging and the coupling efficiency was slightly worse than directly bonding the optical fiber to the aluminum wire using phenyl salicylate (by a factor of two). This was due, in large part, to the difficulty of phase matching the multiple aluminum wires (3). Despite these challenges, the split horn is a much more robust design than the others we had tested for commercial or military deployment. It allows safe positioning of the acoustic waveguides without causing strain on the optical fibers and can be installed after or during fiber deployment by personnel with limited training. Therefore, we chose the focus our efforts on the implementation of the horn methodology for this reporting period.

3.3.9 Theoretical Modeling of the Horn Structure

Multiple designs of horns were investigated in this project to enhance the coupling efficiencies between the acoustic waveguide and the optical fiber. To eliminate the reflections due to abrupt geometry changes, the designed horn structure includes a front horn as well as a back horn, making it a dual horn structure. An array of simulations and experiments were performed to evaluate biconical and bi-exponential tapering structures.

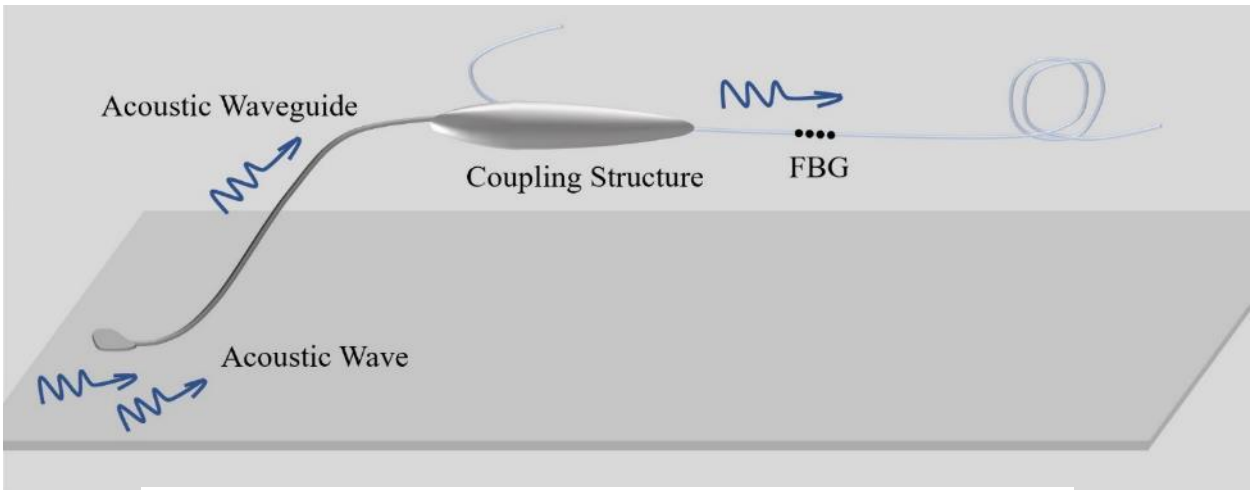

Figure 28. Illustration of the horn design.

An illustration of acoustic coupling to an optical fiber via a horn is shown in Figure 28. An aluminum wire was used as the acoustic waveguide to capture the energy from the testing piece, the aluminum plate in this case, to the back-horn section. The energy will then propagate through the base section to the front horn section and finally is guided to an optical fiber with FBGs for acoustic detections. The horn structure allows for inherent design flexibilities including the choice of acoustic waveguide because it permits geometry and material mismatch between the acoustic waveguide and optical fiber. The acoustic waveguide thus has broad possibilities of materials and dimensions. In addition, this structure potentially allows multiple acoustic waveguides coupling to the horn. As the acoustic waveguide increases its diameter and quantities, the area of acceptance increases, therefore the total energy of the received is expected to be increased.

A modal analysis of the guided modes in the aluminum wire was performed to better understand and optimize the horn structure, as shown Figure 29. In the low frequency range, the longitudinal mode L_{01}, flexural mode F_{11} and torsional mode T_{01} (not plotted) coexist in the aluminum wire. As the frequency increases, higher order modes (e.g., L_{02}) appear in the aluminum wire, which complicates our analysis. At the same time, as the product of the frequency and radius increases, the radial component of L_{01} will also increase. To maximize the axial component of the L_{01} mode

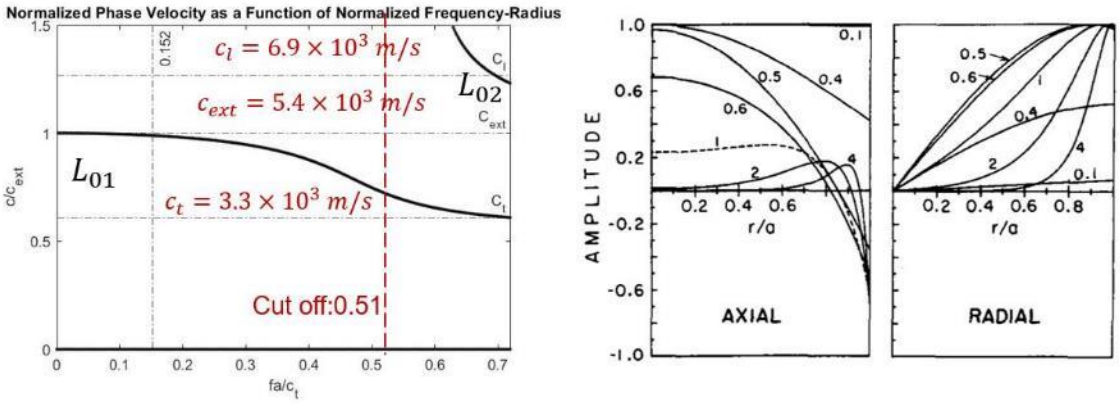

Figure 29. (a) Normalized phase velocity as a function of the product of frequency and radius for the longitudinal modes in the aluminum wire. (b) Axial and radial component distribution as a function of the product of radius and frequency for L_{01} mode.

but maintain the large diameter of the acoustic waveguide, 24AWG aluminum wire was chosen in our experiment, corresponding to 0.152 of the normalized frequency radius products.

The geometry of the biconical horn structure is shown in Figure 30. The parameters of the horn were swept via numerical simulations with COMSOL Multiphysics. The diameter (r) and the

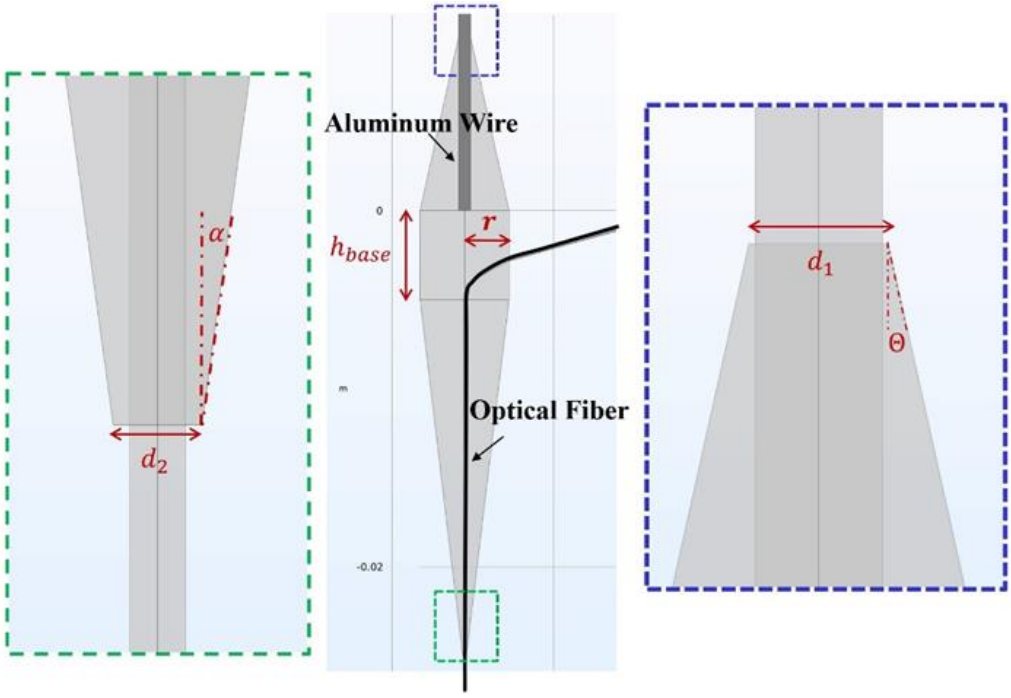

Figure 30. The geometry of the biconical horn

length of the base section (h_{base}) as well as the tapering angles of the back horn (θ) and front horn (α) varied in the analysis to investigate the coupling efficiency dependence on these parameters. In actual fabrication attempts, the tip diameters of the horn do not perfectly match with the wire and the optical fiber, thus the dependency of coupling efficiency on the mismatch at the back horn (d_1) as well as the front horn (d_2) were investigated. In the simulation, the aluminum wire is 24 AWG, and the optical fiber is bare fiber with a 125 μm diameter. The polyimide coating as well as the coupling adhesive is not included in the simulation for simplicity.

The total energy transferred in the acoustic waveguide is unknown in the current experimental measurements. To evaluate the coupling efficiency of the horn, the direct coupling case was included as a reference case, where the acoustic energy was transmitted directly from the aluminum wire to the optical fiber. With the reference case, the simulated strain and energy components from the horn simulations are normalized by the value of the direct coupling case with the same excitations. In the following sections, the normalized transfer efficiency refers to the transfer efficiency of the horn case normalized by the direct coupling case. The geometry of the direct coupling between the aluminum wire and the optical fiber is illustrated in Figure 31. The optical fiber and the aluminum wire maintain the same dimensions as in the horn simulations, and the optical fiber and the aluminum wire share a 5 mm interaction section. Since FBGs are mostly sensitive to axial strain, the excitation and probing in the simulation mostly focus on axial strains. The simulation results for sweeping the horn geometries are shown in Figure 32.

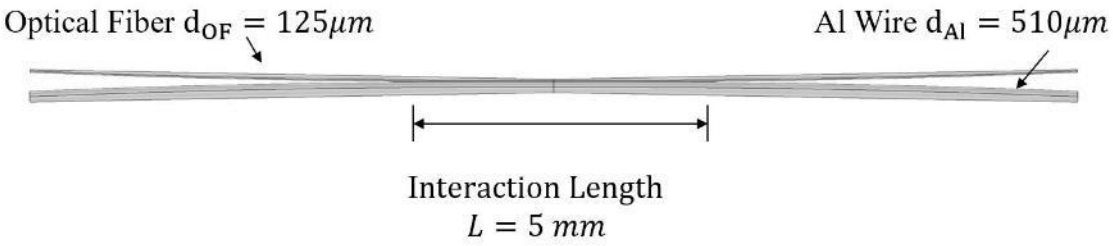

Figure 31. The geometry of direct coupling structure.

The coupling efficiency has negligible dependence on the base length, as it is shown in Figure 32(a). The tapering angles of both the front horn and the back horn were investigated with the sweeping of the horn radius, as it is shown in Figure 32(b) and Figure 32(c). The simulation results show that for both tapering structures, a smaller tapering angle (slower tapering rate) will enhance the coupling efficiency as the horn has better impedance matching. In addition, the smaller radius of the horn gives, higher coupling efficiency because there is less mismatch between the radius of

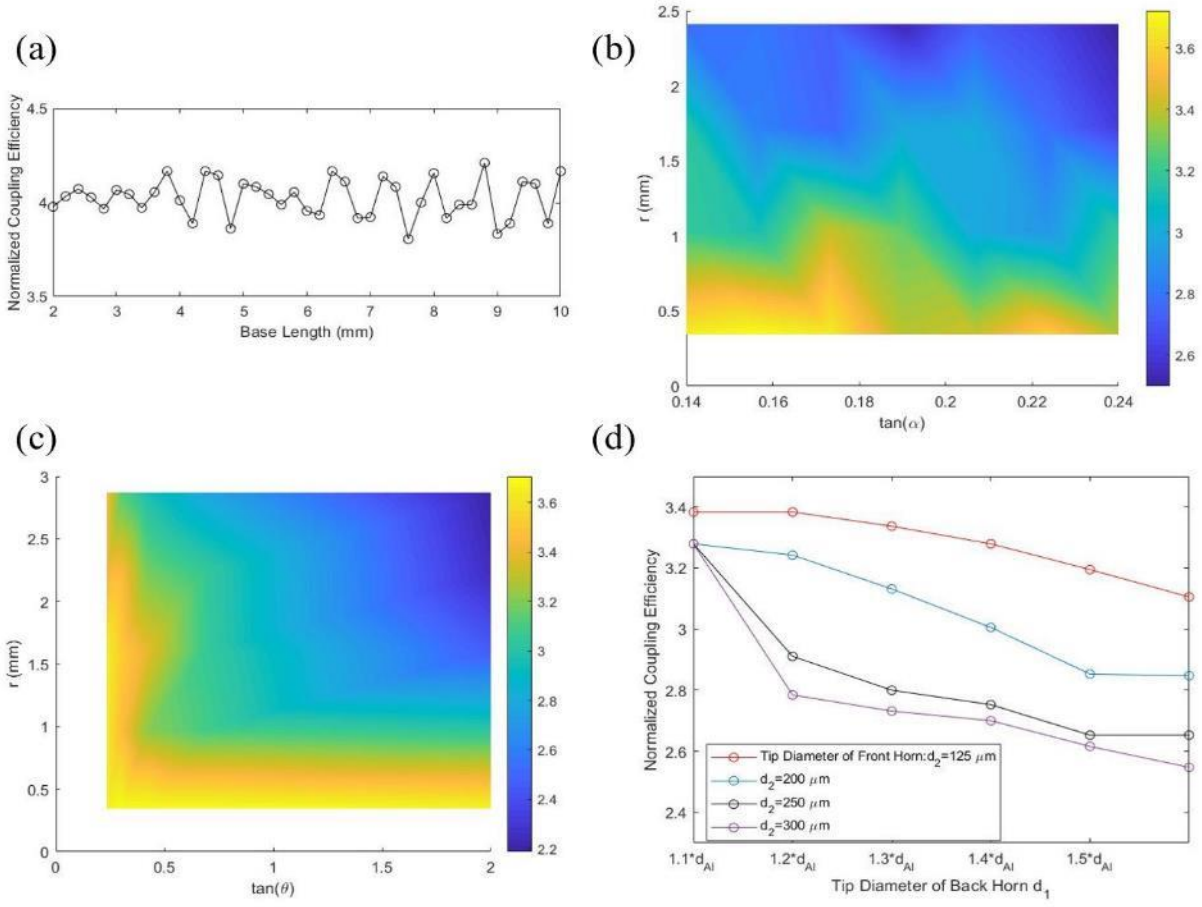

Figure 32. Simulated normalized coupling efficiency dependence on (a) base length, (b)horn radius and back horn tapering angle, (c) horn radius and front horn tapering angle (d), and mismatch at the horn tips.

the acoustic waveguide and the horn. The simulation results for the mismatch between the horn tip and acoustic and optical waveguide are shown in Figure 32(d); as anticipated, the mismatch at the horn tip will compromise the coupling efficiencies. The dimensions of the final design, as it is shown in Table 1, were selected based on several factors including the in-house machining capabilities, the hardness of the aluminum material and ease of the implementation.

Table 1. Dimensions of the biconical horn design

	Radius	Base Length	Back Horn Length	Front Horn Length
Dimensions(mm):	2.5	5	10	20

The frequency responses of the horn structure and the comparison with the direct coupling case were also investigated. The frequency response of the normalized coupling efficiency and the absolute strain value in the optical fiber with 1Pa boundary load along the axial direction of the aluminum wire are shown in Figure 33. Within the broadband region (0.4MHz to 2.2MHz), the normalized coupling efficiency is always above unity, which indicates that the horn structure shows better performance compared with direct coupling. The normalized coupling efficiency as

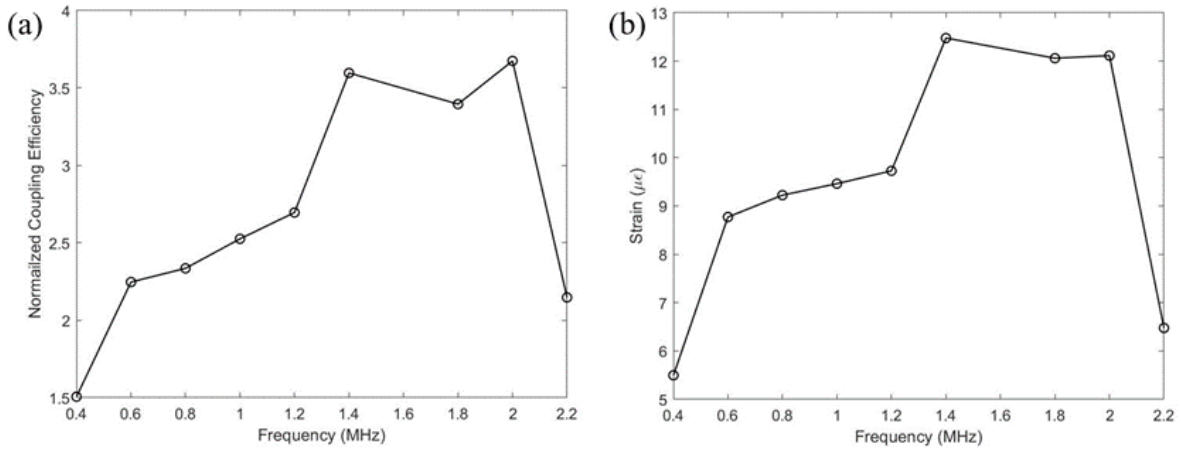

Figure 33. (a) Simulated normalized coupling efficiency as a function of frequencies. (b) Simulated axial strain as a function of frequencies.

well as the absolute strain with a constant load show maximized efficiency at around 1.4~2MHz with decreased coupling efficiency at lower and higher frequencies. In the high frequency range, the assumption that the longitudinal mode is mostly composed of the axial component is not valid which will diminish the coupling efficiency.

To further improve the coupling efficiency, the exponentially tapering structure was also investigated. Compared to the biconical structure where the horn tapers linearly, the bi-exponential horn provides better impedance matching at the tip when the horn diameter approaches the diameter of the aluminum wire and the optical fiber. The geometry of the exponential horn is illustrated in Figure 34(a) which shares the same geometry as it is shown in Table 1, but with an exponential tapering profile. The simulation results in Figure 34(b) show the bi-exponential horn have better coupling efficiency than the biconical designs. In actual fabrication attempts, the aluminum wire was inserted into the slot/hole at the back horn and there are two different methods for the implementation of the optical fiber. The first method is splitting the horn into two halves

and the optical fiber was placed into the slot sandwiched in between them. The second method includes a slot on one side of the horn, and the optical fiber was inserted to the side slot, as it is shown in Figure 34(a). Due to the sharp tip of the exponential horn, the alignment of the split horn is practically difficult and side slot horn is adopted for implementation. The simulated strain response of the side slot horn at 1 MHz is plotted in Figure 34(b) with that of the bi-exponential horn without a slot and the biconical horn. The decreased in coupling efficiency compared with the no-slot case results from the abrupt geometry change at the side slot. It is anticipated that the real coupling efficiency will be better than is shown in the simulations because the applied adhesive will fill the gap of the slot and holes. Biconical horns and the bi-exponential horns were designed, fabricated, and tested to evaluate performance.

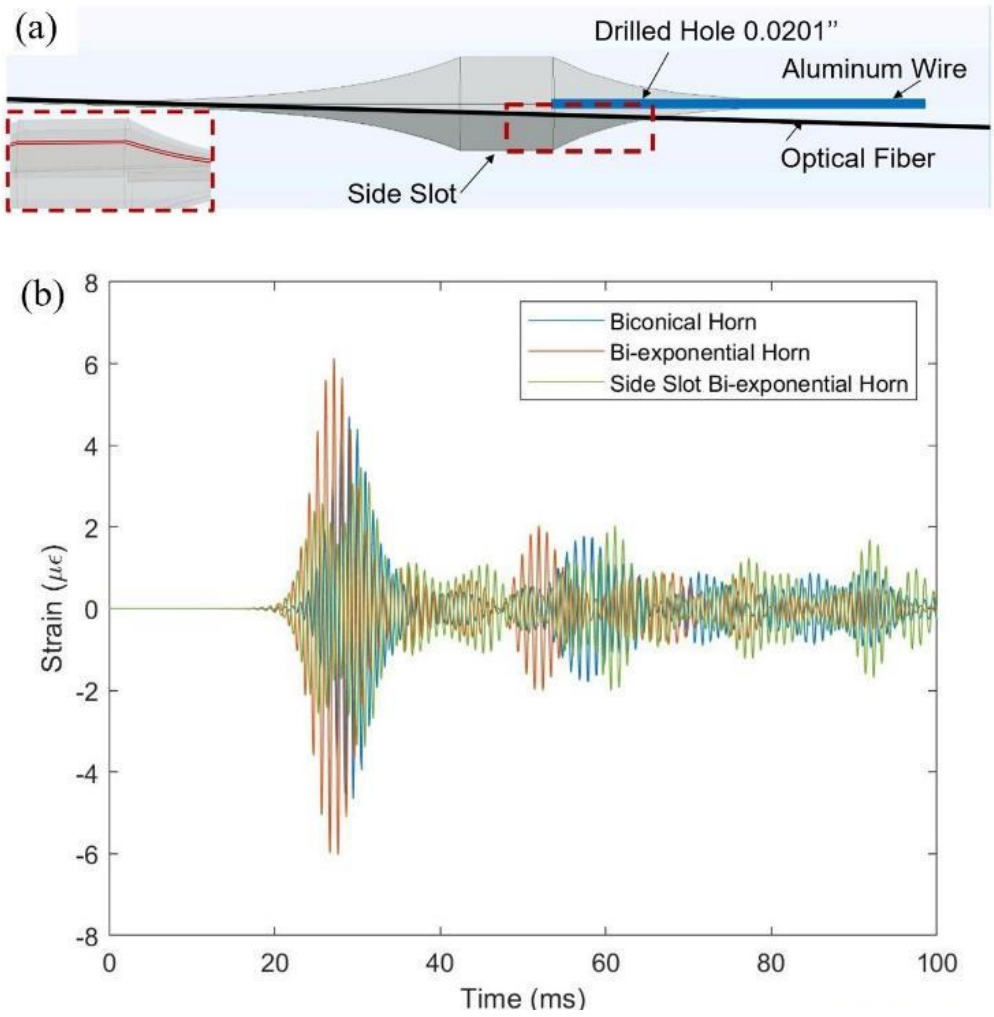

Figure 34. (a) Schematic of the side slot horn structure. (b) Comparison of the simulated strain traces for biconical horn, bi-exponential horn and bi-exponential horn with a side slot.

3.3.10 Fabrication and Characterization of horns

To verify the accuracy of the simulation results, the biconical and bi-exponential horns were fabricated and characterized.

3.3.10.1 Biconical Horn Characterization and Fabrications

The biconical horns were fabricated by our in-house machine shop. Two halves of the horn were machined to the desired shape by computer numerical control milling (Tormach, PCNC 101), as shown in Figure 35(a). The two halves of the horn were then polished by sandpaper to eliminate acoustic scattering due to the rough boundaries. Afterwards, the grooves for optical fiber were engraved onto one half of the horn and the slot at the back horn for the aluminum wire was engraved on both halves of the horn by a laser marker system (FM-Station, Boss Laser), as shown in Figure 35(b). The surface profiler and microscopic images of the slot in the back horn and front horn are included in Figure 35(c) and (d), respectively.

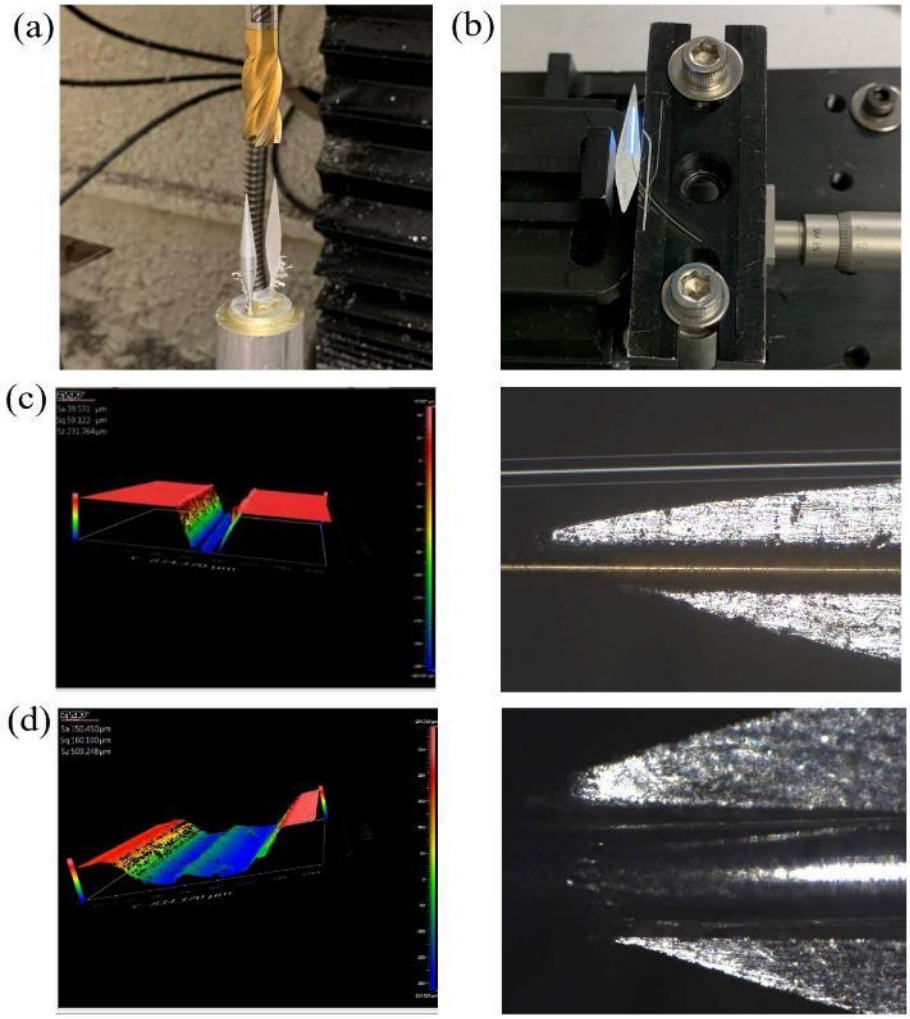

Figure 35 (a) CNC machining (b)Slot engraving by laser marker. Surface profiler image of the slots on the front (c) and back horn (d) respectively.

The experimental setup for the acoustic detection is shown in Figure 36. One side of the aluminum was crushed to a flat tapering structure by the lab press to couple more energy from the aluminum plate and the other side was polished to a flat surface for the horn assembly. The polished aluminum wire was then inserted into the slot at the back side of the horn and the optical fiber was

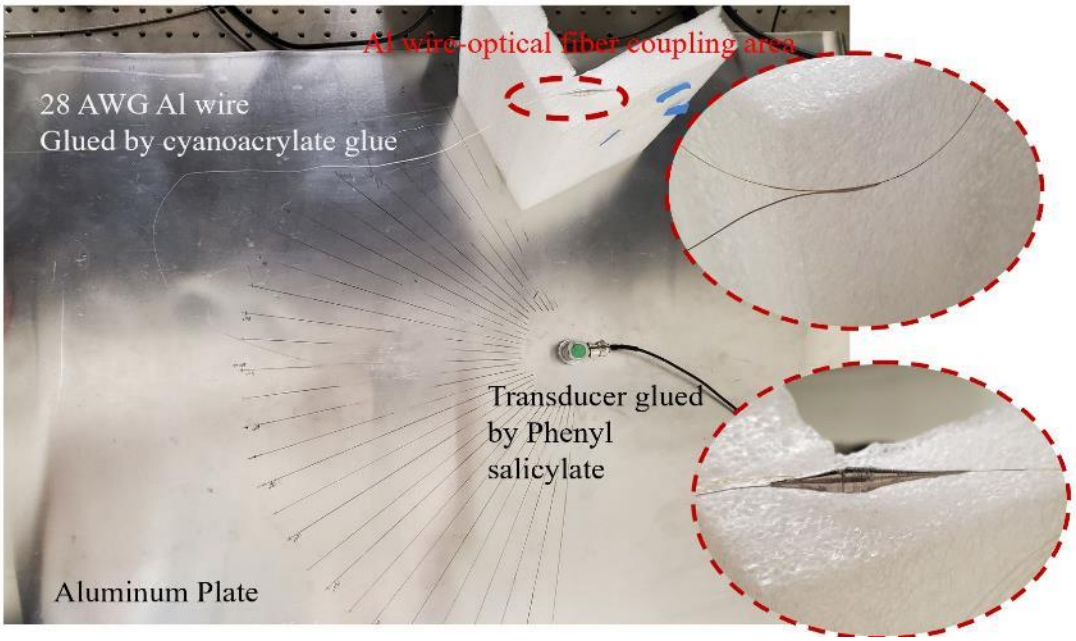

Figure 36. Aluminum wire captures signal from the test piece, and then couples to the optical fiber by direct coupling or biconical horn (inserted image).

inserted into the slot at the front horn. Afterwards, melted phenyl salicylate was applied to fill the gaps and another half of the horn was pressed to sandwich the aluminum wire and the optical fiber in between. The assembled horn was gently placed onto a foam to isolate the ultrasonic transmission path from the plate directly to the horn. The transducer was bonded onto the aluminum plate with phenyl salicylate. The couplings of aluminum wire and the transducer to the aluminum plate were kept the same between trials. The optical fiber was connected to the interrogation system and output traces were averaged 1000 times to increase the signal to noise ratio.

As it is shown in Figure 37(a), the peak-to-peak amplitude of the strain detected in both coupling

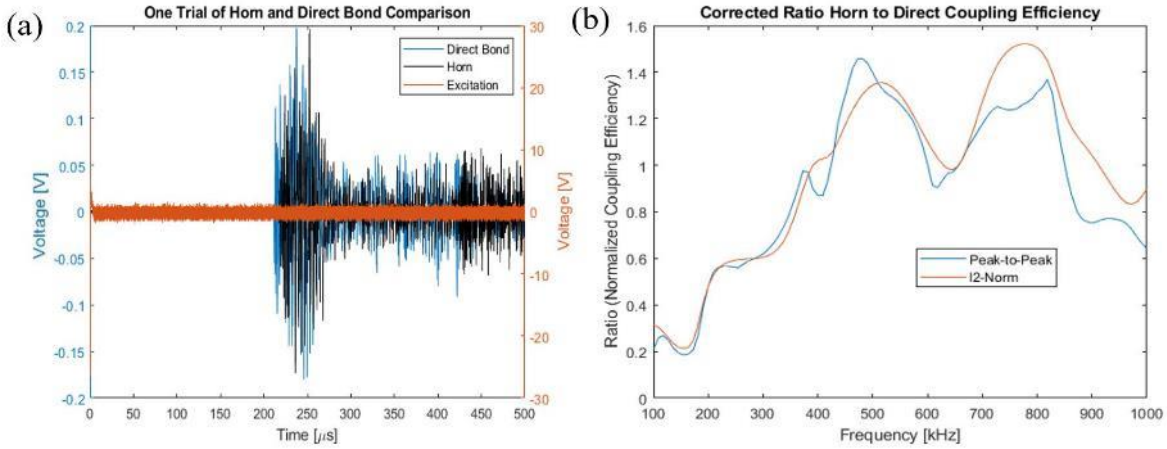

Figure 37. (a) One trial of biconical horn and direct coupling comparison. (b) Frequency dependent normalized peak to peak value and the l-2 norm value.

methods observes similar amplitudes, the ratio of horn to direct bonding peak to peak amplitude is recorded as 0.99. However, further analysis on the frequency dependent responses (Figure 37(b)) shows that in frequency range of 400~800 kHz, the ratio of horn to direct bonding is larger than unity, showing enhancement of the coupling efficiency from the horn couplings.

3.3.10.2 Bi-exponential Horn Fabrication and Characterization

To further improve the coupling efficiency of the biconical horn, a bi-exponential horn structure was proposed and verified by the experimental results. Due to the difficulty of alignment for two halves of the horn, a side slot structure was adopted to ease the process of implementation. Following the same procedures of the fabrication as the biconical horn, the exponential horn was first fabricated by CNC, then a 10 mm-deep hole was drilled by the microdrill bit (Figure 38(a)), and a side slot was cut by a 0.006" silicon carbide cutting wheel (Contenti) following a programmed path, as it is shown in Figure 38(b). The microscopic image of the horn tip shown in Figure 38(c) verified good matching between the side slot and the optical fiber.

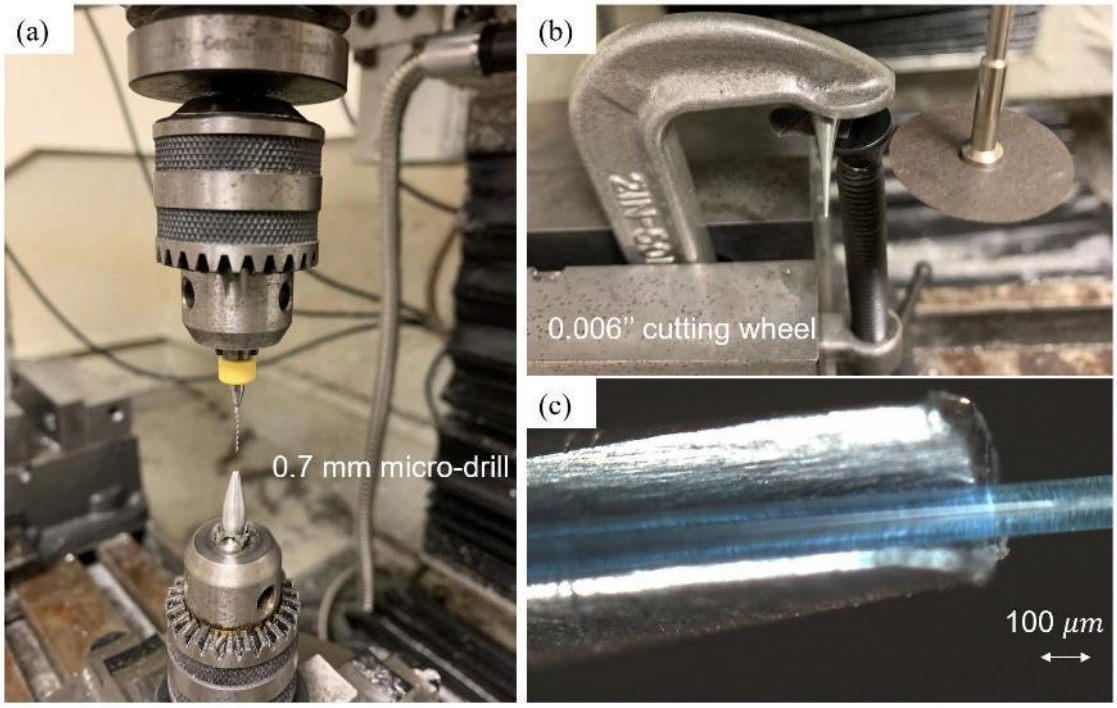

Figure 38. (a) Drill a hole at the back horn section by microdrill bit. (b) Side slot fabrication with an ultrathin cutting wheel. (c) Microscopic image of the horn tip with optical fiber inside the slot.

A procedure for the side slot horn assembly was also developed to improve the repeatability and precision of the implementation. The horn was first ultrasonic cleaned by acetone and then clamped by a homemade vise to a fixed position. As it is shown in Figure 39(a), fiber was clamped by two clamps on both side of the horn and the fiber position was adjusted until it fully seated inside the slot. The aluminum wire was gently inserted to the hole until it reached the bottom of the back horn. Melted phenyl salicylate was applied to seal the gap between the optical fiber, wires and the horn. The whole setup was then placed inside a vacuum chamber, shown in Figure 39(b). After reheating the horn with a heat gun to remelt the adhesive, the assembled horn was degassed

inside the chamber until the phenyl salicylate fully crystalized. Afterwards, the horn was transferred on to a piece of foam for testing, as shown in Figure 39(c). The bi-exponential horn was tested with the same setup as for other horns. The initial results showed that the bi-exponential horn exhibited a better coupling efficiency compared with the biconical horn. As shown by the time domain analysis in Figure 39(d), the normalized peak-to -peak coupling efficiency is 1.089. and the normalized l-2 norm ratio is 1.4082, showing that 50% more energy was transmitted through the horn structure compared with the direct coupling case. The periodogram in Figure 39(e) and the frequency dependent coupling ratio plotted in Figure 39(f) show the analysis of the

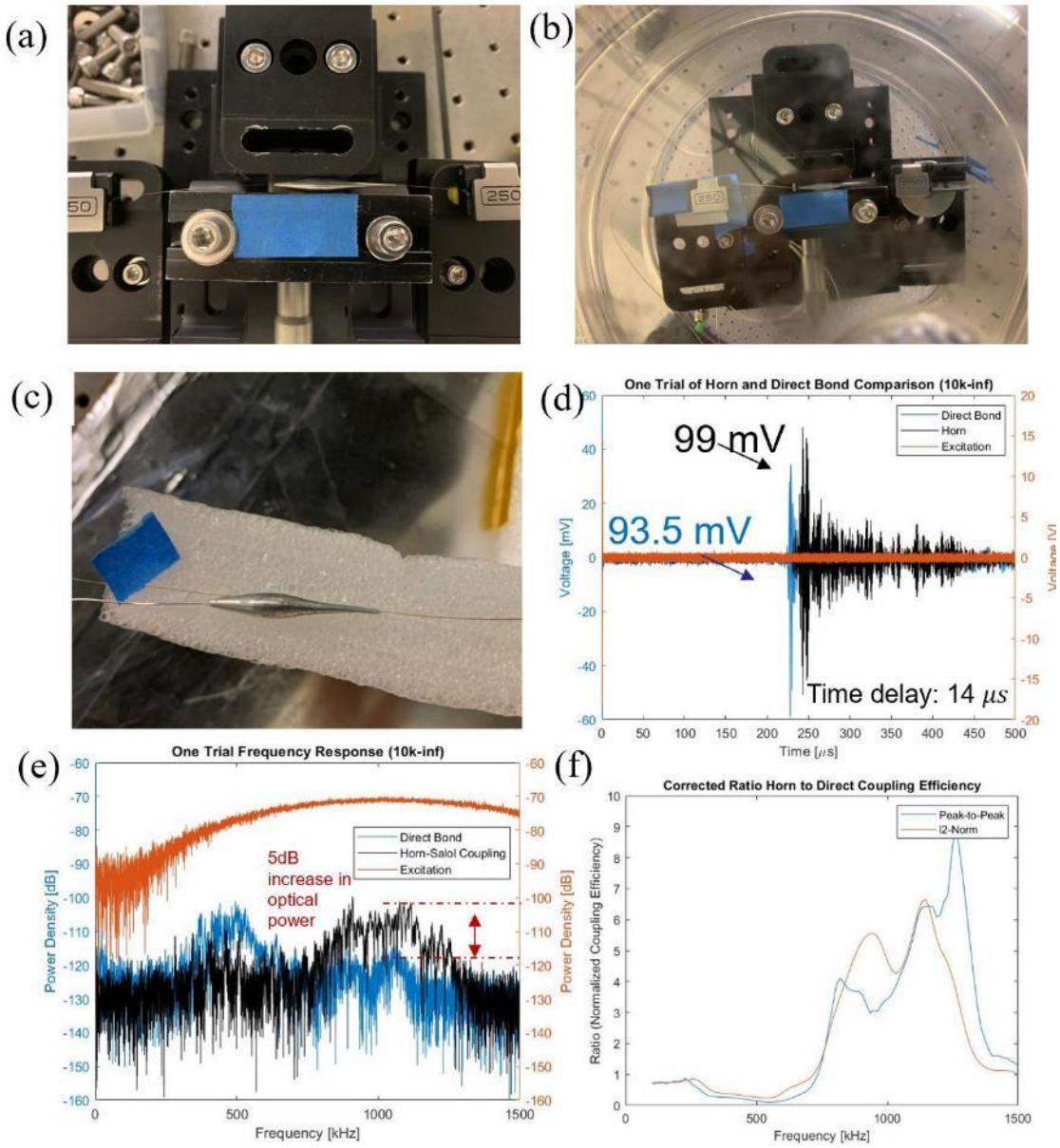

Figure 39. Side slot horn assembling procedures. (a) Fiber alignment with the horn and (b) degassing procedure. (c)Assembled side slot horn. (d) One trial of bi-exponential horn trace compares with one trial of direct coupling trace. (e) Periodogram of the horn and direct coupling traces. (f) Normalize coupling efficiency as a function of frequencies.

frequency dependency on the coupling methods. Considering the application on the structural health monitoring, we are more interested in the frequency response between 0.2~2 MHz. The horn coupling structure shows a 5dB increase in optical power at around 1 MHz where the direct coupling case has better performance at lower frequencies. The frequency dependent peak to peak amplitude ratio shown in Figure 39(f) leads to a similar conclusion, where the horn has better coupling efficiency in both peak-to-peak amplitude and energy value above 600 kHz.

3.3.11.1 Wire Horn Fabrication and Characterization

While dual-horn structures can efficiently match the impedance and geometry discontinuity of two waveguides, there are factors that diminish the coupling efficiency:

(1) The difficulties with horn assembly. As a joint between the acoustic waveguide and optical fiber, the assembly process of the dual horn is vulnerable to error and inaccuracy, any mismatch or trapped air bubbles within the horn structure can compromise the coupling efficiency. The complexity of the assembly process can be an issue for field implementation.

(2) Multiple reflection points in the structure. Although the tapering structure is designed to avoid geometrical mismatches, the limited accuracy of the machining can introduce multiple reflection joints.

Therefore, new designs that can simplify the assembly procedure and involve less reflection joint are needed. Here, we proposed 'wire horn structure', where the ultrasonic waveguide is 'one-piece' with the tapering structure. The ultrasonic waveguide is directly tapering down from the original diameter to the diameter that can match with the optical fiber. Compared with the dual-horn structure where the acoustic energy was first guided to a larger diameter, this 'one-piece' tapering down structure can maximize the energy coupling efficiencies.

One example of the wire horn structure is shown in Figure 40(a), a large diameter aluminum wire was slowly tapered into a wedge shape. The other side of the aluminum wire, not included in this plot, was flattened to maximize the energy coupling from the aluminum plate to aluminum waveguide. On the wedged side of the wire horn, a groove with a width close to the fiber diameter, was machined for optical fiber embedding, which allows the energy coupling from the wire horn structure to the optical fiber.

The numerical simulation of the wire horn structure was analyzed in COMSOL. Considering the machinability, the 12 AWG wire was chosen in the simulation. Following the same rule of normalization, the horn coupling structure was compared with the directly coupling case. The transmitted axial strains by direct coupling case and horn case are plotted in Figure 40(b), showing that the wire horn structure enhanced the coupling efficiency by 2.65 times. The zoomed-in image of the strain energy distribution is plotted in Figure 40(c), showing the energy concentration and distributed impedance matching at the tapering structure. Without the assembly between the acoustic waveguide and the horn structure, the only possible reflection point due to abrupt

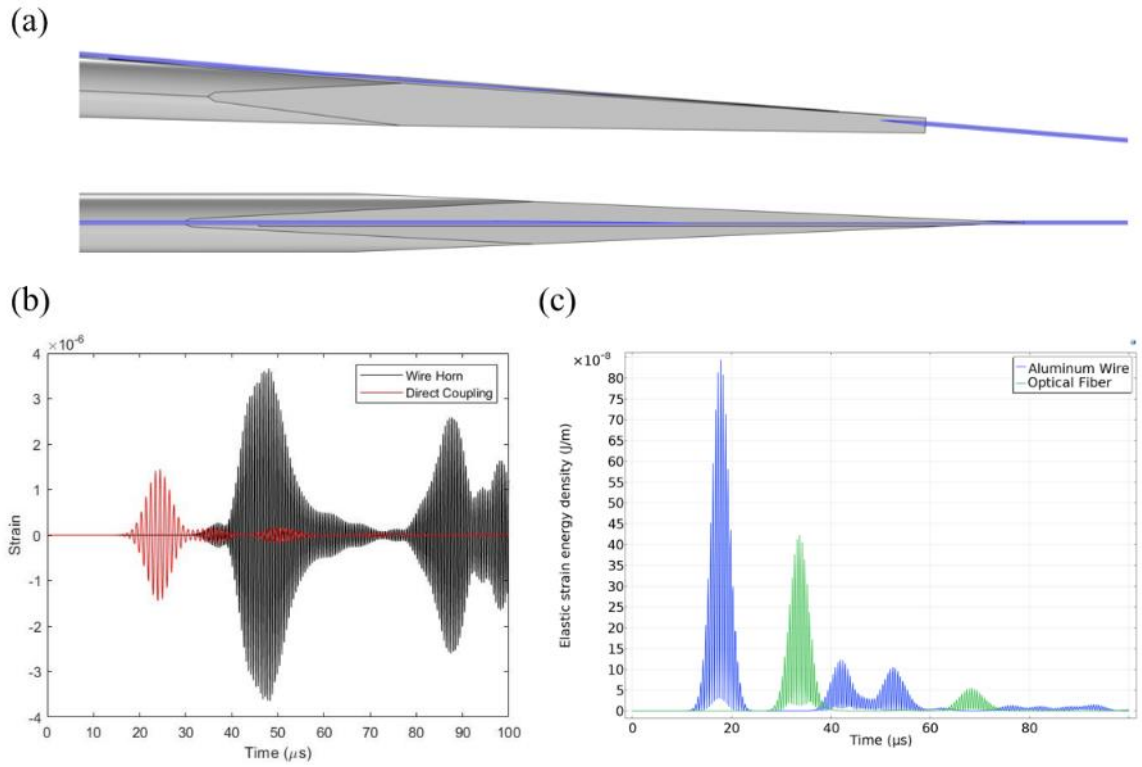

Figure 40. (a) Schematic of wire horn structure. (b) Comparison of the simulated axial strain for the wire horn and direct coupling. (c) Energy density integrated over aluminum wire and optical fiber cross sectional area.

geometry change is the joint between the optical fiber and the tip of the wired horn. The ratio of the reflection to transmission can be calculated by integrating the strain energy density on the waveguide cross-sectional area. The reflection ratio of the wire horn structure is 14.8% showing the decrease in reflection by using the wire horn structure.

To understand the coupling efficiency's dependency on the geometry, simulations on different wire diameters, horn tapering angles are investigated.

The structure of the wire horn is determined by wire diameter, horn tapering angle and horn tip angle. The horn tapering angle and horn tip angles act together to determine the tapering rate of the wire horn. For 12AWG aluminum wire with a constant input energy load, the integrated energy over the fiber cross-section was plotted in Figure 41(a) when varying the horn tip angle. Here, the horn tapering angle was kept as 3° as a constant value and horn angles increases leading to a faster tapering structure. As shown in the graph, the energy transmitted to optical fiber decreases as the horn tip angle increases. This is a similar trend found in dual-horn simulations. The faster tapering rate will have worse impedance match and leads to higher reflections as the ultrasonic wave enters the horn structure. The results of normalized coupling efficiency as a function of the wire diameter are included in Figure 41(b). With the same boundary load per unit area, the input energy of the wire horn increases parabolically as the wire diameter increases. To view how the energy transfer efficiency changes as the wire diameter increases, the ratio of the axial component was normalized by the total energy input into the wire. The monotonically decrease trend indicates the larger

diameter of the wire horn compromised the coupling efficiency as there are more mismatch between the initial wire diameter and the fiber diameter. In addition, the larger wire dimeter will lead to a larger axial component in the aluminum wire which makes the conversion to the axial component in the optical fiber less efficient. However, as the aluminum wire increases its radius, the total energy input increases, therefore there are two beating effects to decide the total energy been transmitted to optical fiber. With the assumption of constant energy input per unit area, the maximum energy transfer to the optical fiber reaches its peak when the diameter of the aluminum wire is 2 mm, which is the plot of $\int E(OF)dS$ shown in Figure 41(c). The integration of the axial

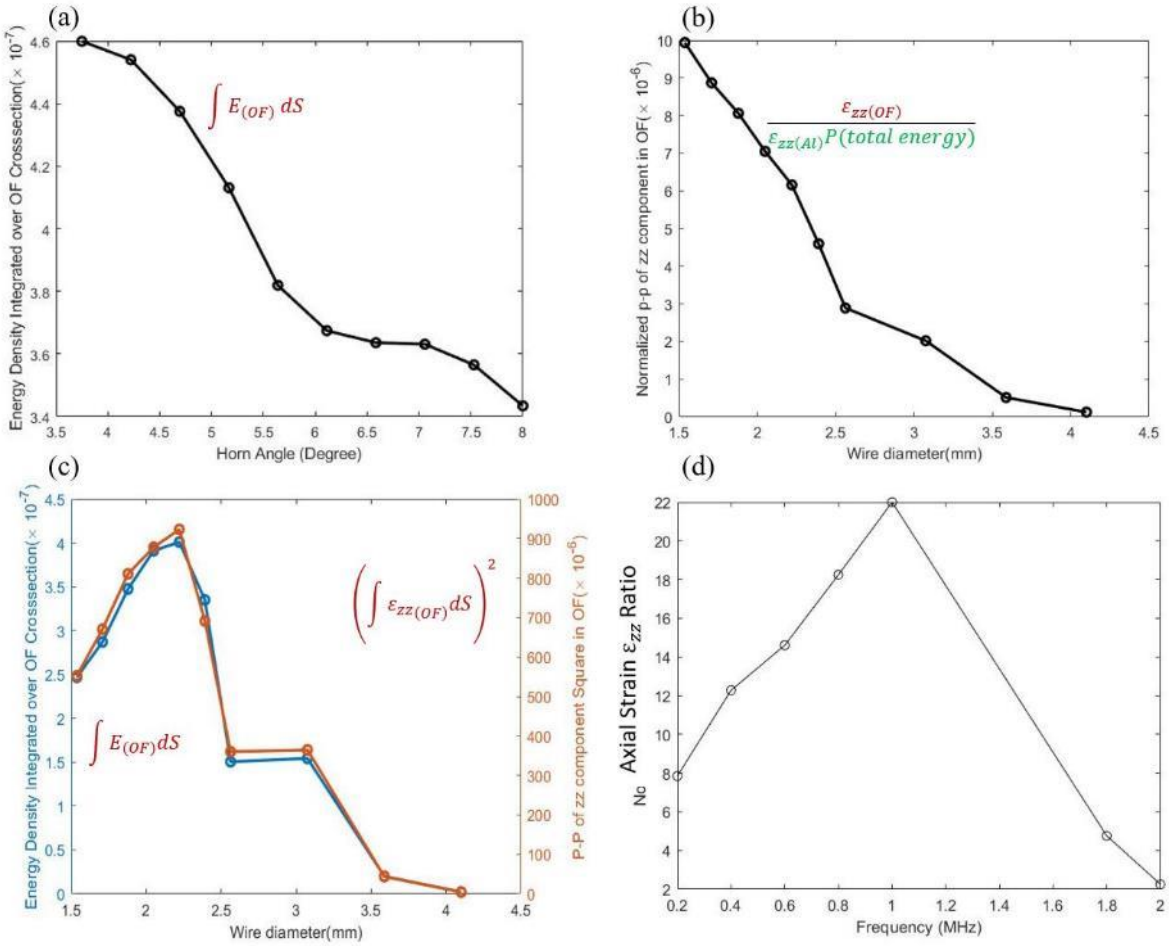

Figure 41. Simulation results of different wire horn structures (a) Integrated energy density over optical fiber cross-sectional area as a function of horn angles. (b)(c) Coupling efficiency as function of horn wire diameter. (d) Frequency response of the wire horn.

displacement in the optical fiber is plotted as the red trace in the same graph. The overlapping between the total energy input and the axial components shows the percentage of the axial component is not a function of the wire diameter. In figure 41(d), the frequency response of the wire horn was investigated: The wire horn shows larger than 2 times enhancement over frequency range 0.2~2 MHz, and shows maximum enhancement at 1MHz, which is the central frequency of the structural health monitoring applications.

3.3.11.2 Wire Horn Fabrication and Characterization

To verify our idea, we utilized in-house machine facilities for the fabricating of the wire horn. The 12 AWG aluminum wire was first flattened by the lab press on both ends, creating a gradual transition from a round wire surface to a flattened surface. The tapering angle is decided by angle between the top and bottom surface of the lab press and is 3° in this case. After flattening two end surfaces of the aluminum wire, one end of the flattened surface was chosen to be the wire horn. The flattened section was cut by the laser marker shown in Figure 42(a) with designed horn angle θ, where the horn angle was chosen to be 5° for the initial test. A groove was also engraved by the

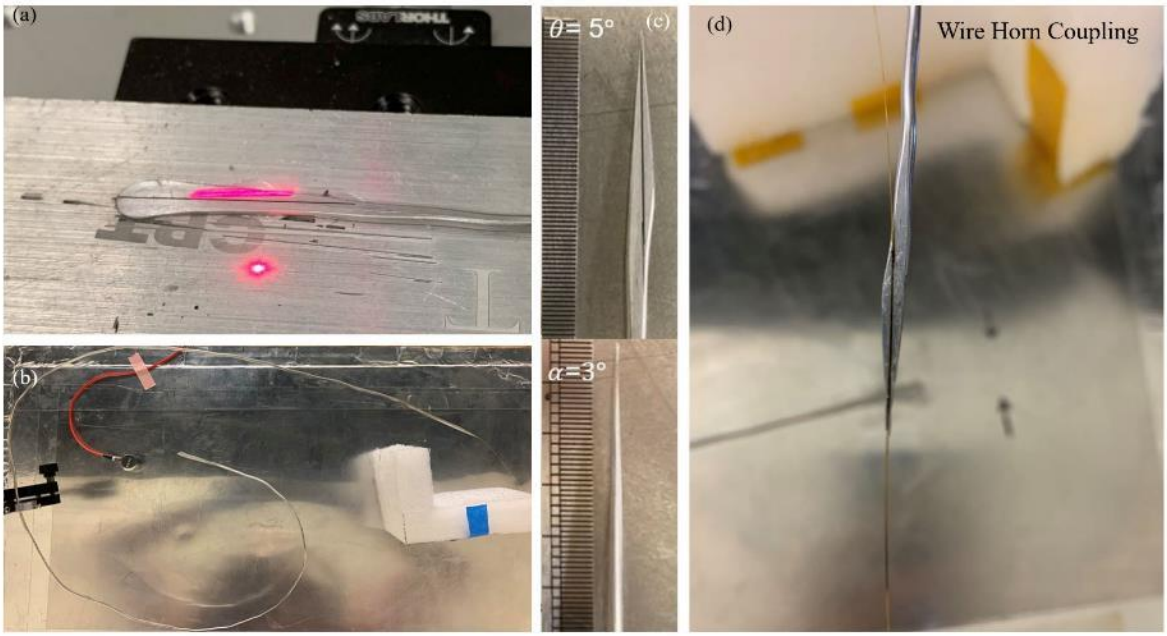

Figure 42. (a) Laser marker was used to cut wire horn. (b) Wire horn testing setup. (c) A fabricated wire horn sample. (d) Optical fiber glued into the trench of the wire horn.

laser marker, with width around 200 μm, to accommodate the optical fiber in the horn structure. The fabricated wire horn was shown in Figure 42(c) with optical fiber embedded. The testing setup is shown in Figure 42(b), one end of the wire horn was glued to the aluminum surface with adhesive, and the optical fiber was pushed into the slot of the wire horn and glued by UV adhesive (cyanoacrylate). The amount of the UV adhesive should be precisely controlled to enable a good acoustic coupling between the aluminum wire and optical fiber and minimize the acoustic attenuation due to the excessive amount of the cyanoacrylate adhesive. A 5mm third order fiber Bragg Grating is a few millimeters away from the wire horn tip and the reflected signal from the FBG was recorded by the same electro-optical system described in previous sections. An additional direct coupling test was performed as a reference to the wire horn coupling case. As it is shown in Figure 43(a), the peak-to -peak amplitude of the wire horn is 7.9 and 5.5 times respectively. The normalized $l2$ norm value of the horn structure is 5.93 and 3.8 times larger than the two cases of the direct coupling. In addition, the measured signal was also plotted in the frequency domain, Figure 43(b) to investigate the frequency dependent response of the wire horn.

The wire horn coupling structure shows an averaged 5dB enhancement across the frequency of interest, indicating the broadband enhancement of the coupling efficiency.

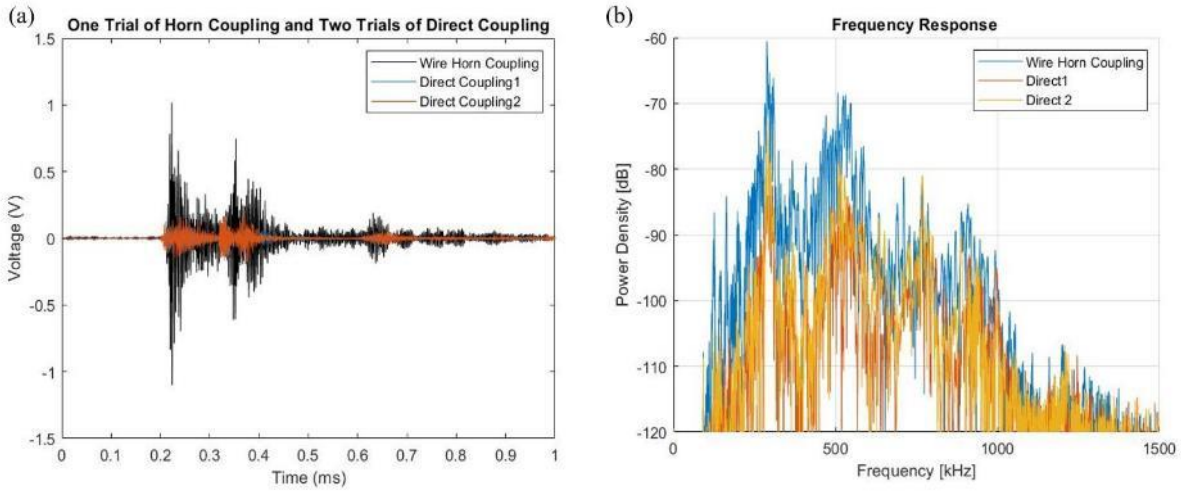

Figure 43. (a) Measured time domain traces for wire horn coupling and direct coupling. (b) Periodogram of the wire horn coupling and direct coupling, indicating broadband enhancement

3.4 Training and Professional Development

Training and professional development is one of the many core objectives for the principal investigators (PI) of this project. The intense collaborative effort required to perform the work in this project accelerated the "hands-on" education of the students as well as provide the unique experience of working with a very diverse team**.** The students working in this project developed the necessary communication skills via publications of their work in peer reviewed journals and presentations at selected conferences. The mentoring of junior faculty by the principal investigator promoted the professional development of the next generation of faculty members at domestic universities.

Dr. Gary Pickrell, Lead PI, and Dr. Anbo Wang, co-PI, mentor Dr. Daniel Homa, in all aspects of research project management, as well as providing the skills and experience necessary to help mentor the students working on the project. The faculty at Virginia Tech worked directly with the students, providing guidance on the planning, execution and analysis of laboratory experiments via the scientific method. The graduate research assistants, Shuo Yang, Ruixuan Wang and Logan Theis performed the theoretical analyses and conducted all the experimental work. Furthermore, the students were required to present the results of their ongoing work at the bi-weekly meetings and generate research reports which provide consistent opportunities for them to develop their scientific writing and presentation skills. The students presented the results of their work to the Program Manager in regularly scheduled meetings and upon request.

4 PARTICIPANT & OTHER COLLABORATING ORGANIZATIONS

The research conducted over the three-year project was performed by the Center for Photonics Technology (CPT) at Virginia Tech via active collaboration between the Bradley Department of

Electrical and Computer Engineering (ECE) and the Department of Materials Science and Engineering at Virginia Tech.

1	Type	Co-Investigator
2	Prefix (optional)	Dr.
3	First Name	Gary
4	Last Name	Pickrell
5	Middle Name (optional)	---
6	Suffix (if applicable)	---
7	Nearest person month worked	1
8	National Academy Member? (Y/N)	N
9	Country if participant is a foreign collaborator	N/A

1	Type	Co-Investigator
2	Prefix (optional)	Dr.
3	First Name	Anbo
4	Last Name	Wang
5	Middle Name (optional)	---
6	Suffix (if applicable)	---
7	Nearest person month worked	1
8	National Academy Member? (Y/N)	N
9	Country if participant is a foreign collaborator	N/A

1	Type	Faculty
2	Prefix (optional)	Dr.
3	First Name	Daniel
4	Last Name	Homa
5	Middle Name (optional)	---
6	Suffix (if applicable)	---
7	Nearest person month worked	1
8	National Academy Member? (Y/N)	N
9	Country if participant is a foreign collaborator	N/A

5 STUDENTS

Three graduate research assistants, Shuo Yang, Logan Theis, and Ruixuan Wang, all from the ECE department, were participants in the project. Dr. Yang successfully defended his Ph.D. dissertation in 2020 and accepted a post-doc position at another University. Prior to his departure, Mr. Theis worked closely with Dr. Yang to ensure a smooth transition for the work that was performed in the second project year. Ruixuan Wang conducted all the theoretical and experimental work in the final year of the project.

6 PRODUCTS

One conference paper titled 'Efficient Acoustic-Optical Fiber Coupling with Wire Horn Structure' was accepted will be presented in the upcoming FiO + LS 2023 conference. Two manuscripts are to be for submitted for publication in a peer reviewed journal. Two intellectual property disclosure were submitted to Virginia Tech Intellectual Properties (VTIP) for consideration for filing with the United States Patent Office.

7 MILESTONE STATUS

The goals, objectives and the statuses of the project milestones are captured by the approved project milestones shown in Table 1. Overall, the project is on schedule and on budget.

Table 1. Project Milestone Status

#	Milestone Title & Description	Planned Completion Date	Actual Completion Date	Comments
1	Project Management Plan	5/19/20	5/15/20	Completed.
2	Theoretical Horn and Coupler Design and Analysis	10/19/20	9/30/20	Completed
3	Coupler Fabrication and Characterization	4/19/21	12/30/20	Completed
4	Evaluation of Acoustic Coupling to Single Crystal Sapphire Fiber	4/19/21	4/10/21	Completed
5	Design and Testing of Fiber Optic – Acoustic Sensor	10/19/21	10/19/21	Completed
6	Design and Assembly of Prototype SHM System	4/19/22	4/19/23	Completed
7	SHM System Integration and Performance Testing	4/19/23	4/19/23	Completed
8	Final Report	8/18/23	8/18/23	Completed